

Cellular Traffic Offloading Through Tethered-UAV Deployment and User Association

Osama M. Bushnaq, *Student Member, IEEE*, Mustafa A. Kishk, *Member, IEEE*,
Abdulkadir Çelik, *Senior Member, IEEE*, Mohamed-Slim Alouini, *Fellow, IEEE*,
and Tareq Y. Al-Naffouri, *Senior Member, IEEE*.

Abstract

Unmanned aerial vehicles (UAVs) have recently received a significant interest to assist terrestrial wireless networks thanks to their strong line-of-sight links and flexible/instant deployment. However, UAVs' assistance is limited by their battery lifetime and wireless backhaul link capacity. At the expense of limited mobility, tethered UAVs (tUAVs) can be a viable alternative to provide seamless service over a cable that simultaneously supplies power and data from a ground station (GS). Accordingly, this paper presents a comparative performance analysis of tUAV and regular/untethered UAV (uUAV)-assisted cellular traffic offloading from a geographical area that undergoes heavy traffic conditions. By using stochastic geometry tools, we first derive joint distance distributions between the hot-spot users, the terrestrial base station (TBS), and the UAV. To maximize the end-to-end signal-to-noise ratio, a user association policy is developed, and corresponding association regions are analytically identified. Then, the overall coverage probability of the uUAV/tUAV-assisted system is derived for given locations of the TBS and the uUAV/tUAV. Moreover, we analytically prove that optimal UAV location falls within a partial surface of the spherical cone centered at the GS. Numerical results show that tUAV outperforms uUAV given that sufficient GS locations accessibility and tether length are provided.

Keywords

Unmanned aerial vehicle (UAV); tethered UAV; stochastic geometry; hot-spot coverage; user association; traffic offloading.

Authors are with Computer, Electrical, and Mathematical Sciences and Engineering (CEMSE) Division at King Abdullah University of Science and Technology (KAUST), Thuwal, 23955-6900, KSA.

I. INTRODUCTION

UNMANNED aerial vehicles (UAVs) have rapidly gained a tremendous interest to be used in numerous emerging commercial and military applications such as aerial surveillance, border protection, traffic control, transportation, logistics, precision agriculture, search & rescue missions, disaster recovery, etc. In particular, UAV-based airborne communications bring a major paradigm shift to the information and communication technology (ICT) sector, which primarily depends upon a terrestrial communication and networking infrastructure [1], [2]. Indeed, UAVs can offer salient attributes to today's fixed telecom infrastructure, including strong line-of-sight backhaul/access links, flexible/instant deployment, and extra degrees of freedom for the controlled mobility [3].

In the context of wireless communications, the ambitious quality-of-service demands (i.e., high-rate, ultra-reliable, and low-latency) of the next-generation networks can be fulfilled by UAV-assisted cellular communications, whereby UAVs are integrated with the terrestrial cellular infrastructure for various applications. In this regard, UAVs have been recently envisioned as aerial base stations [4], relays [4]–[6], user equipments (UE) [7], and data fusion access points [8]–[11]. Thanks to UAV's instant and cost-efficient deployment, UAV-assisted cellular communication is especially suitable for providing extra coverage to geographical regions that experience heavy traffic conditions, which are also referred to as *hot-spots*. Unless this heavy traffic is caused by an extraordinary event (e.g., natural disasters), hot-spots generally follow a spatio-temporal pattern that is caused by mass events such as sports matches, concerts, conferences, exhibitions, demonstrations, etc. Unlike the high cost of deploying fixed terrestrial base station (TBS) to serve these occasional or periodic events, UAVs can hover over the hot-spot and assist the existing TBSs to provide ground users with better coverage.

Nonetheless, utilizing UAVs as aerial base stations has two main drawbacks: Firstly, the limited capacity of state-of-the-art batteries poses a daunting challenge for the operational lifetime of UAVs. Therefore, a UAV cannot be available throughout the entire mission duration as it is required to return to a charging/docking station, charge/replace its battery, and return back to the hot-spot region. Secondly, the service quality offered to the hot-spots is restricted by the capacity of the backhaul link between the UAV and TBS. Although UAV is fully flexible to be deployed anywhere, the backhaul link capacity restrains its deployment region to a space around the TBS. Tethered UAVs (tUAVs) can be a viable alternative to supply both power and data over a cable

from a ground station (GS), which can be located on a rooftop or a mobile station [12]. Given a set of accessible GS locations, tUAVs can also fly between GSs to serve hot-spots that do not overlap in the temporal domain. Nevertheless, the tUAVs are also susceptible to the following limitations [13]: Firstly, the optimal GS location may not be readily available. Therefore, the number of GS location (e.g., building density) and their accessibility (i.e., the permission of the residents) has an impact on the optimal deployment strategies. Secondly, the tether length and inclination angle of the tUAV restrain the freedom of mobility around the GS. At this point, it is worth noting that the backhaul link capacity of a regular/untethered UAV (uUAV) plays the role of tether by limiting the distance from the TBS. Considering that both systems have virtues and drawbacks, the main objective of this paper is to provide a comparative performance analysis of uUAV and tUAV-assisted cellular traffic offloading under the practical challenges¹.

A. Related Work

Since the limited energy supply at the UAV forms a critical challenge for the deployment of the aerial BSs, energy-efficient UAV communication is studied in [14]. However, it is shown in [2], [3], [15] that the communication power is negligible compared to the mechanical power consumed during hovering and traveling. Therefore, improving the communication power efficiency has a negligible impact on the overall UAV energy efficiency. The propulsion power consumption can be reduced by controlling the UAV speed and hovering height [16], [17]. In [17], the UAV propulsion energy and communication related energy are minimized while satisfying a throughput constraint for the served users. Battery replacement/recharging approaches are proposed in [18]–[20], where solutions can significantly improve the uUAV availability at the expense of extra cost and complexity.

Deployment of aerial BSs is studied in [21]–[23]: In [21], the number of UAVs is minimized such that a group of ground users is in the coverage range of at least one UAV. Similarly, the UAV is placed to maximize the number of users covered by the UAV and the quality of the A2G link in [22]. In [23], a relaying UAV is placed optimally to minimize the overall outage and bit error rate. In [24], a stochastic geometry analysis is provided to place multiple UAVs such that the coverage probability over a hot-spot is maximized. In order to improve the overall user QoS, the backhaul link and the association policy must be carefully studied. In [6],

¹Throughout the paper, the term ‘UAV’ is used to refer both uUAVs and tUAVs.

the UAV-assisted network is assessed, assuming a mmWave backhauling for a random ground BS and UAV locations. In [25], point-to-point free-space optics (FSO) links are proposed for UAV backhaul/fronthaul connection. In [26], the UAV placement problem is solved to maximize the data rate while considering limited backhaul and radio access capacity. Unlike the above works dealing with the deployment of uUAVs, we consider tUAV deployment and compare its performance with uUAV under practical scenarios.

The practical advantages of tUAVs were recently discussed in [12]. These advantages include (i) having a stable power supply through the tether connecting the UAV to the GS and (ii) having a reliable wired data-link connecting the UAV to the GS. In [13], the average path-loss for a point-to-point link between a tUAV and a ground user was derived and optimized. In [27], the authors proposed a novel UAV-based communication system for a post-disaster setup. In particular, uUAVs are used for providing cellular service for disaster areas, while tUAVs are used to provide backhaul links for the uUAVs. Unlike existing literature, this paper focuses on optimizing the tUAV placement to provide cellular service for multiple ground users. To achieve that purpose, we use tools from stochastic geometry to model the locations of the ground users. This is motivated by the tractability of stochastic geometry tools and their ability to provide closed-form expressions for various performance metrics [28]–[30]. More details on the contributions of this paper are provided next.

B. Main Contributions

The main contribution of the paper is summarized as follows:

- A stochastic geometry based analysis is provided for coverage performance of uUAVs and tUAVs over a circular hot-spot region where UEs are uniformly distributed. While uUAVs are limited by being available for a given duty cycle period, tUAVs are restrained by a maximum tether length, inclination angle, and GS location accessibility.
- The joint probability density functions (PDFs) are derived for the distances among UEs, the TBS, and the UAV. To maximize the end-to-end system coverage, a user association policy is developed and association regions are identified based on the distance PDFs. Finally, we provide the overall coverage probability of uUAV and tUAV-assisted cellular networks.
- Since the search space of the deployment area is very large, we analytically prove that optimal UAV location falls within the surface of the spherical cone centered at the GS.

Finally, extensive simulation results are presented to validate analytical results and compare the performance of uUAV and tUAV-assisted systems.

C. Paper Notations and Organization

We refer the readers to Table I for the list of notations. The remainder of the paper is organized as follows: Section II explains the considered system model and characterizes access and backhaul links. Section III derives the joint distance PDFs and obtains the coverage probabilities. Section IV analytically derive the optimal hovering space. Then, Section V presents the numerical results. Lastly, Section VI concludes the paper with a few remarks.

II. SYSTEM MODEL

We consider improving downlink wireless coverage in highly crowded areas with heavy traffic conditions, which is referred to as *hot-spots* throughout the paper. The hot-spot region is modeled as a disk centered at the origin \mathbf{L}_o with radius R_o , $\mathcal{D}(\mathbf{L}_o, R_o) \subset \mathbb{R}^2$, where UEs are assumed to be uniformly distributed. Without loss of generality, the TBS location $\mathbf{L}_b = \{x_b, 0, h_b\}$ is assumed to be at the x -axis for the sake of presentation. To this end, we aim at offloading downlink traffic from a TBS to an uUAV or a tUAV. The uUAV is a regular UAV that can freely hover at any location in \mathbb{R}^3 . However, it has a defined flight duration due to the limited lifetime of state-of-the-art battery technology. Therefore, its service availability is modeled by a duty-cycle parameter $\xi \in [0, 1]$ which is determined based on charging and serving durations of the uUAV. Another restrain on the uUAV is the limited capacity of the backhaul link between the TBS and the uUAV, which has a critical impact on deployment and user association strategies as overall coverage probability is jointly determined by access (UAV–UE) and backhaul (TBS–UAV) links. On the other hand, the tUAV is connected to a ground station (GS) which uninterruptedly supplies both power and data through a tether. The GSs can be installed on N potential rooftops whose locations are denoted by $\mathbf{L}_n = \{x_n, y_n, h_n\}$, $n \in [1, N]$. On the negative side, the mobility of tUAV is restrained by its maximum tether length T and minimum inclination angle ϕ . As a result, the reachability of tUAV is restricted to the following spherical cone

$$\mathcal{M}_n = \left\{ x_u, y_u, h_u : \|\mathbf{L}_n - \mathbf{L}_u\| \leq T, \arcsin \left(\frac{h_u - h_n}{\|\mathbf{L}_n - \mathbf{L}_u\|} \right) \geq \phi \right\}, \quad (1)$$

where the GS location \mathbf{L}_n is the center of spherical cone and $\mathbf{L}_u = \{x_u, y_u, h_u\}$ is the location of the tUAV. Considered system model is demonstrated in Fig. 1.

TABLE I: Summary of the notations.

Notation	Description
$\{\cdot\}_r/\{\cdot\}_b/\{\cdot\}_u$	Subscripts refer to the RUE/TBS/UAV
\mathbf{L}_i	Location of an arbitrary point i
$D_{i,j}$	Euclidean distance between \mathbf{L}_i and \mathbf{L}_j , $D_{i,j} \triangleq \ \mathbf{L}_i - \mathbf{L}_j\ $
$\{\cdot\}'$	Ground projection of a point or a distance
$\mathcal{L}(\mathbf{L}_i, \mathbf{L}_j)$	The line segment formed by connecting the points at \mathbf{L}_i and \mathbf{L}_j
$\angle(\mathbf{L}_i, \mathbf{L}_j, \mathbf{L}_k)$	The angle at \mathbf{L}_j formed by moving from $\mathcal{L}(\mathbf{L}_i, \mathbf{L}_j)$ to $\mathcal{L}(\mathbf{L}_j, \mathbf{L}_k)$ counterclockwise
\mathbf{L}_x^+	A point in the positive x direction, i.e., $\mathbf{L}_x^+ = \{\infty, 0, 0\}$
$\mathcal{C}(\mathbf{L}_i, R_i)$	Circle centered at \mathbf{L}_i with radius R_i
$\mathcal{D}(\mathbf{L}_i, R_i)$	Disk centered at \mathbf{L}_i with radius R_i
$\mathcal{A}(\mathbf{L}_j, R_j, \mathbf{L}_i, R_i) \subseteq \mathcal{C}(\mathbf{L}_j, R_j)$	Arc centered at \mathbf{L}_j with radius R_j within $\mathcal{C}(\mathbf{L}_i, R_i)$
$\ \cdot\ $	ℓ_2 norm
$ \cdot $	Absolute value for scalars or Lebesgue measure for sets

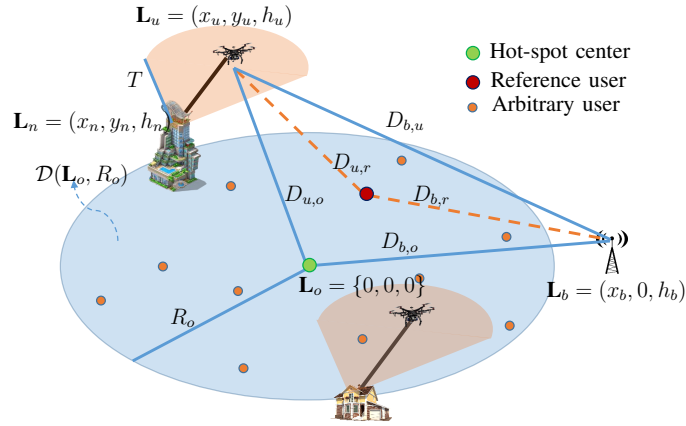


Fig. 1: Data offloading through tUAV system model.

In the rest of the paper, we will focus our analysis on a reference UE (RUE), which is randomly selected from the disk $\mathcal{D}(\mathbf{L}_o, R_o)$ and located at \mathbf{L}_r . In the following subsections, we characterize the terrestrial access link between the TBS and the RUE, air-to-ground (A2G) aerial access link between the UAV and the RUE, and ground-to-air (G2A) aerial backhaul link between the TBS and the uUAV.

A. Terrestrial Access Links (TBS–RUE)

The TBS→RUE access link is assumed to experience free-space path-loss as well as Rayleigh fading. As a result of path-loss, the transmitted signal power decays with distance, i.e., $D_{b,r}^{-\alpha_b}$ where $D_{b,r} = \|\mathbf{L}_b - \mathbf{L}_r\|$ is the three dimensional (3D) Euclidean distance between the TBS and RUE, and α_b is the path-loss decay exponent. Accordingly, the signal to noise ratio (SNR) at the RUE is expressed as

$$\text{SNR}_{b,r} = \frac{\rho_b G_{b,r} D_{b,r}^{-\alpha_b}}{\sigma_n^2}, \quad (2)$$

where $G_{b,r}$ is the channel gain, ρ_b is the TBS transmission power, and σ_n^2 is the noise variance. Following from the Rayleigh fading assumption, $G_{b,r}$ is exponentially distributed with the probability density function (PDF) $f_{G_{b,r}}(g) = \mu e^{-g\mu}$, where μ is the fading parameter.

B. Aerial Access (UAV–RUE) and Backhaul (TBS–uUAV) Links

Both aerial access and backhaul links are assumed to experience free-space line-of-sight (LoS) and non-line-of-sight (NLoS) attenuation path-loss as well as Nakagami- m fading. The probability of having a LoS transmission between a UAV and an arbitrary location is given by

$$\kappa_{u,i}^{\text{LoS}} = \prod_{k=0}^K \left(1 - \exp \left(- \frac{\left(h_u - \frac{(k+0.5)(h_u - h_i)}{K+1} \right)^2}{2\gamma_1^2} \right) \right), \quad (3)$$

where $K = \lfloor D_{b,i} \sqrt{\gamma_2 \gamma_3} - 1 \rfloor$ and γ_i is the environmental parameter such that γ_1 , γ_2 and γ_3 represent building heights distribution, the ratio of built up land to the total land area, and the average number of buildings per km^2 , respectively [31]. If the TBS height is fixed to h_b , (3) can be approximated for the TBS–uUAV backhaul link as follows [32],

$$\kappa_{b,u}^{\text{LoS}} = \left(1 + a_b \exp \left[-b_b \left(\arcsin \left(\frac{h_u - h_b}{D_{b,u}} \right) - a_b \right) \right] \right)^{-1}, \quad (4)$$

where a_b and b_b are approximation parameters depending on h_b , γ_1 , γ_2 and γ_3 . Similarly, the LoS probability between the UAV and the RUE, which is at height $h_r = 0$, can be approximated as,

$$\kappa_{u,r}^{\text{LoS}} = \left(1 + a_r \exp \left[-b_r \left(\arcsin \left(\frac{h_u}{D_{u,r}} \right) - a_r \right) \right] \right)^{-1}, \quad (5)$$

where a_r and b_r are depending on h_r , γ_1 , γ_2 and γ_3 .

Following the Nakagami- m fading assumption, the G2A/A2G channel gain $G_{i,j}$ between two arbitrary points \mathbf{L}_i and \mathbf{L}_j is Gamma distributed with the PDF

$$f_{G_{i,j}}(g) = \frac{m^m g_u^{m-1}}{\Gamma(m)} \exp(-m), \quad (6)$$

where $\Gamma(\cdot)$ is the gamma function. While setting $m = 1$ models the Rayleigh fading, the Rician fading is approximated by setting $m > 1$ [33]. Given the aforementioned G2A/A2G channel

characteristics, the signal to noise ratio (SNR) for the aerial access link is expressed as

$$\text{SNR}_{u,r} = \frac{\rho_u G_{u,r} D_{u,r}^{-\alpha_u}}{\sigma_n^2 \eta_k}, \quad (7)$$

where ρ_u is the UAV transmission power and $\eta_k, \forall k \in \{\text{LoS}, \text{NLoS}\}$, are the attenuation coefficients for the LoS/NLoS links. Likewise, the SNR of the aerial backhaul link between the TBS and uUAV is expressed as

$$\text{SNR}_{b,u} = \frac{\rho_u G_{b,u} D_{b,u}^{-\alpha_u}}{\sigma_n^2 \eta_k}. \quad (8)$$

While the uUAV acts as a relay between the RUE and the TBS, the tUAV is directly connected to the core network via a fiber optics packed high-speed ultra-reliable link. Therefore, we assume for the tUAV that $\text{SNR}_{b,u} \gg \text{SNR}_{u,r}$ holds all the time.

C. Association Policy

The RUE associates with the TBS or the UAV based on which one provides a higher average access link SNR². Accordingly, in case of LoS and NLoS aerial access links, the RUE respectively associates with the UAV if it is located within the following areas,

$$\mathcal{B}_{\text{LoS}}^u = \left\{ x_r, y_r : \overline{\text{SNR}}_{b,r} < \overline{\text{SNR}}_{u,r}^{\text{LoS}} \right\} = \left\{ x_r, y_r : D_{u,r} \leq \left(\frac{D_{b,r}^{\alpha_b}}{\eta_{\text{LoS}}} \right)^{\frac{1}{\alpha_u}} \right\}, \quad (9)$$

$$\mathcal{B}_{\text{NLoS}}^u = \left\{ x_r, y_r : \overline{\text{SNR}}_{b,r} < \overline{\text{SNR}}_{u,r}^{\text{NLoS}} \right\} = \left\{ x_r, y_r : D_{u,r} \leq \left(\frac{D_{b,r}^{\alpha_b}}{\eta_{\text{NLoS}}} \right)^{\frac{1}{\alpha_u}} \right\}, \quad (10)$$

where $\overline{\text{SNR}}_{b,r}$ and $\overline{\text{SNR}}_{u,r}^k, k \in \{\text{LoS}, \text{NLoS}\}$, are the average SNRs for terrestrial and aerial access links, respectively. Notice in (9) and (10) that we always have $\mathcal{B}_{\text{NLoS}}^u \subset \mathcal{B}_{\text{LoS}}^u$ due to the fact that $\eta_{\text{LoS}} < \eta_{\text{NLoS}}$.

III. COVERAGE PERFORMANCE ANALYSIS

Throughout this section, we focus our attention on a randomly located RUE within the hot-spot region, i.e., $\mathbf{L}_r \in \mathcal{B}_o$. As a result of randomness, we first derive necessary distance distributions between the TBS/UAV and the RUE. Then, coverage performance of access and backhaul links are analyzed by using these distance distributions as building blocks.

²Here, we assume that the RUE is agnostic to the backhaul link conditions.

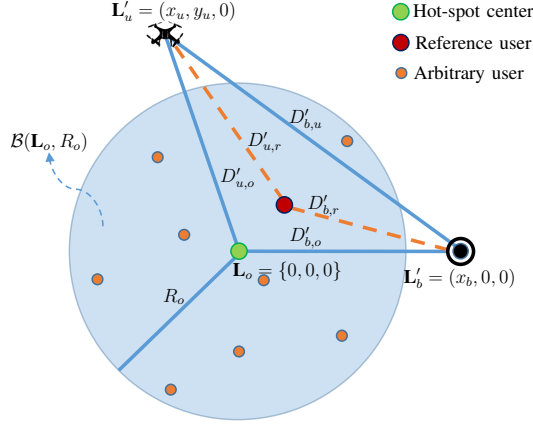


Fig. 2: Aerial view of the system model in Fig. 1.

A. Distance Distributions

Coverage performance is primarily determined by two joint factors: SNR levels of access/backhaul links and user association resulting from the SNR levels. It is obvious from (2), (7), and (8) that the SNR levels are highly dependent on the RUE's random location and thus its random distance to the TBS and the UAV, i.e., $D_{b,r}$ and $D_{u,r}$, respectively. In what follows, we consider projected distances over $x - y$ plane for the sake of a better presentation. As illustrated in Fig. 2, projected distances are defined as $D'_{b,r} \triangleq \sqrt{D_{b,r}^2 - h_b^2}$ and $D'_{u,r} \triangleq \sqrt{D_{u,r}^2 - h_u^2}$. Likewise, a projected location of an arbitrary point is denoted by $\mathbf{L}'_i \triangleq \{x_i, y_i, 0\}$. To derive the coverage probability, one first need to compute the joint PDF of $D'_{b,r}$ and $D'_{u,r}$ as well as their marginal PDFs. To this end, we provide formal definitions of a line segment, circle and arc as follows.

Definitions: The line segment connecting the points \mathbf{L}_i and \mathbf{L}_j is defined as $\mathcal{L}(\mathbf{L}_i, \mathbf{L}_j) \triangleq \overline{\mathbf{L}_i \mathbf{L}_j}$. Likewise, the circle centered at \mathbf{L}'_i with radius R_i is defined as

$$\mathcal{C}(\mathbf{L}'_i, R_i) = \{x, y : (x - x_i)^2 + (y - y_i)^2 = R_i^2\}. \quad (11)$$

For any two intersecting circles, we define the arc of $\mathcal{C}(\mathbf{L}'_j, R_j)$ located inside $\mathcal{C}(\mathbf{L}'_i, R_i)$ as

$$\mathcal{A}(\mathbf{L}'_j, R_j, \mathbf{L}'_i, R_i) = \{x, y : (x - x_j)^2 + (y - y_j)^2 = R_j^2, (x - x_i)^2 + (y - y_i)^2 \leq R_i^2\}. \quad (12)$$

In the following Lemma, we derive the PDF of the distance between a uniformly distributed point within $\mathcal{D}(\mathbf{L}_o, R_o)$ and any arbitrary point on the $x - y$ plane.

Lemma 1. *The PDF of the distance between a uniformly distributed point \mathbf{L}'_j within $\mathcal{D}(\mathbf{L}_o, R_o)$*

and any arbitrary point \mathbf{L}'_i is given by

$$f_{D'_{i,j}}(r_i) = \begin{cases} \frac{2r_i}{R_o^2} & 0 \leq r_i \leq \max(0, R_o - D'_{i,o}), \\ \frac{2r_i}{\pi R_o^2} \arccos\left(\frac{(D'_{i,o})^2 + r_i^2 - R_o^2}{2D'_{i,o}r_i}\right) & |R_o - D'_{i,o}| \leq r_i \leq R_o + D'_{i,o}, \end{cases} \quad (13)$$

where $D'_{i,o} = \sqrt{x_i^2 + y_i^2}$ is the distance between \mathbf{L}'_i and \mathbf{L}_o .

Proof. Please see Appendix A . ■

Accordingly, the PDF of distance between the RUE and the ground projection of the TBS and the UAV locations can be directly obtained by replacing \mathbf{L}'_b and \mathbf{L}'_u with \mathbf{L}'_i in (13).

Lemma 2. For a given distance between the RUE and the projected TBS location, $D'_{b,r}$, the conditional PDF of distance between a uniformly distributed RUE location $\mathbf{L}_r \in \mathcal{B}(\mathbf{L}_o, R_o)$ and the projected UAV location at \mathbf{L}'_u is given by

$$f_{D'_{u,r}|D'_{b,r}}(r_u|r_b) = \begin{cases} \frac{w}{2\pi r_b} & 0 \leq r_b \leq \max(0, R_o - D'_{b,o}), \quad D'_{b,u} - r_b \leq r_u \leq D'_{b,u} + r_b, \\ \frac{w \mathbb{1}_{\{\check{\theta}_b \leq \check{\theta}_u \leq \hat{\theta}_b\}}}{|\mathcal{A}(\mathbf{L}'_b, r_b, \mathbf{L}_o, R_o)|} & |R_o - D'_{b,o}| \leq r_b \leq R_o + D'_{b,o}, \quad D'_{b,u} - r_b \leq r_u \leq \|\check{\mathbf{L}}_b - \mathbf{L}'_u\|, \\ \frac{w}{2|\mathcal{A}(\mathbf{L}'_b, r_b, \mathbf{L}_o, R_o)|} & |R_o - D'_{b,o}| \leq r_b \leq R_o + D'_{b,o}, \quad \|\check{\mathbf{L}}_b - \mathbf{L}'_u\| \leq r_u \leq \|\hat{\mathbf{L}}_b - \mathbf{L}'_u\|, \\ \frac{w \mathbb{1}_{\{\hat{\theta}_b \leq \hat{\theta}_u \leq \check{\theta}_b\}}}{|\mathcal{A}(\mathbf{L}'_b, r_b, \mathbf{L}_o, R_o)|} & |R_o - D'_{b,o}| \leq r_b \leq R_o + D'_{b,o}, \quad \|\hat{\mathbf{L}}_b - \mathbf{L}'_u\| \leq r_u \leq D'_{b,u} + r_b, \end{cases} \quad (14)$$

where $D'_{b,o} = \|\mathbf{L}'_b\|$, $D'_{b,u} = \|\mathbf{L}'_b - \mathbf{L}'_u\|$, $\mathbb{1}_{\{\cdot\}}$ is the indicator function,

$$w = \frac{2r_u}{D'_{b,u}} \frac{1}{\sqrt{1 - \left(\frac{(D'_{b,u})^2 + r_b^2 - r_u^2}{2D'_{b,u}r_b}\right)^2}}, \text{ and} \quad (15)$$

$$|\mathcal{A}(\mathbf{L}'_b, r_b, \mathbf{L}_o, R_o)| = 2r_b \arccos\left(\frac{(D'_{b,o})^2 + r_b^2 - R_o^2}{2D'_{b,o}r_b}\right). \quad (16)$$

The locations $\check{\mathbf{L}}_b = \{\check{x}_b, \check{y}_b, 0\}$ and $\hat{\mathbf{L}}_b = \{\hat{x}_b, \hat{y}_b, 0\}$ are at the points of intersection between $\mathcal{C}(\mathbf{L}_o, R_o)$ and $\mathcal{C}(\mathbf{L}'_b, r_b)$ expressed as

$$\check{x}_b = \check{x}_b = \frac{R_o^2 - r_b^2 + (D'_{b,o})^2}{2D'_{b,o}} \quad (17)$$

$$\check{y}_b = -\hat{y}_b = \sqrt{R_o^2 - (\hat{x}_b)^2}. \quad (18)$$

Denoting $\mathbf{L}_x^+ = \{\infty, 0, 0\}$ as a point in the positive x direction, $\check{\theta}_b = \angle(\mathbf{L}_x^+, \mathbf{L}_b, \check{\mathbf{L}}_b)$ and $\hat{\theta}_b = \angle(\mathbf{L}_x^+, \mathbf{L}_b, \hat{\mathbf{L}}_b)$ are the angles at \mathbf{L}'_b formed by moving from the line $\mathcal{L}(\mathbf{L}_x^+, \mathbf{L}_b)$ to $\mathcal{L}(\mathbf{L}_b, \check{\mathbf{L}}_b)$ and

$\mathcal{L}(\mathbf{L}_b, \hat{\mathbf{L}}_b)$ counter clockwise. Similarly, $\check{\theta}_u = \angle(\mathbf{L}_x^+, \mathbf{L}_b, \mathbf{L}'_u)$ and $\hat{\theta}_u = (\pi + \check{\theta}_u) \bmod 2\pi$.

Proof. Please see Appendix B . ■

B. Coverage Probability

The coverage probability is defined as the probability that the received SNR is greater than a threshold β . In this subsection, we derive the coverage probability of access and backhaul links for given TBS and UAV locations.

Lemma 3. *For a given SNR threshold β , the coverage probability of the Rayleigh fading terrestrial access link (TBS–RUE) is defined as $P_{b,r}(\beta) \triangleq \mathbb{P}[\text{SNR}_{b,r} > \beta]$ and given by*

$$P_{b,r}(\beta) = \int_{-\infty}^{\infty} P_{b,r|r_b}(\beta) f_{D'_{b,r}}(r_b) dr_b, \quad (19)$$

where $P_{b,r|r_b}(\beta) = \exp(-\bar{\beta}_b(r_b^2 + h_b^2)^{\alpha_b/2})$ is the coverage probability for a given distance to the TBS (r_b), $\bar{\beta}_b = \frac{\sigma_n^2 \beta}{\rho_b}$, and $f_{D'_{b,r}}(r_b)$ is the PDF of distance between \mathbf{L}_b and \mathbf{L}_r [c.f. Lemma 1].

Proof. Please see Appendix C. ■

Lemma 4. *For a given SNR threshold β , the coverage probability of the G2A/A2G Nakagami- m fading aerial access link (UAV–RUE) is defined as $P_{u,r}(\beta) \triangleq \mathbb{P}[\text{SNR}_{u,r} > \beta]$ and given by*

$$P_{u,r}(\beta) = \int_{-\infty}^{\infty} \sum_{i \in \{\text{LoS}, \text{NLoS}\}} \kappa_{u,r}^i P_{u,r|r_u}^i(\beta) f_{D'_{u,r}}(r_u) dr_u, \quad (20)$$

where $P_{u,r|r_u}^i(\beta) = \sum_{k=0}^{m-1} \frac{(m\bar{\beta}_u(r_u^2 + h_u^2)^{\alpha_u/2} \eta_i)^k}{k!} \exp(-m\bar{\beta}_u(r_u^2 + h_u^2)^{\alpha_u/2} \eta_i)$, $\forall i \in \{\text{LoS}, \text{NLoS}\}$, is the LoS/NLoS coverage probability for a given distance to the UAV (r_u), $\bar{\beta}_u = \frac{\sigma_n^2 \beta}{\rho_u}$, and $f_{D'_{u,r}}(r_u)$ is the PDF of distance between \mathbf{L}_u and \mathbf{L}_r [c.f. Lemma 1].

Proof. Please see Appendix D. ■

Corollary 1. *For a given SNR threshold β , the coverage probability of the G2A/A2G Nakagami- m fading aerial backhaul link (TBS–UAV) is defined as $P_{b,u}(\beta) \triangleq \mathbb{P}[\text{SNR}_{b,u} > \beta]$ and given by*

$$P_{b,u}(\beta) = \sum_{i \in \{\text{LoS}, \text{NLoS}\}} \kappa_{b,u}^i \sum_{k=0}^{m-1} \frac{(m\bar{\beta}_u D_{b,u}^{\alpha_u} \eta_i)^k}{k!} \exp(-m\bar{\beta}_u D_{b,u}^{\alpha_u} \eta_i), \quad (21)$$

where $D_{b,u}$ is the distance between the TBS and the UAV.

Proof. This corollary follows by substituting the random RUE location into the deterministic TBS location in Lemma 4. ■

For a given SNR threshold β , the end-to-end coverage probability of the RUE associated with the UAV is defined as $P_{b,u,r}(\beta) \triangleq \mathbb{P}[\min(\text{SNR}_{u,r}, \text{SNR}_{b,u}) > \beta]$ and given by

$$\begin{aligned} P_{b,u,r}(\beta) &= \mathbb{P}((\text{SNR}_{u,r} > \beta) \cap (\text{SNR}_{b,u} > \beta)) \\ &= \mathbb{P}(\text{SNR}_{u,r} > \beta) \mathbb{P}(\text{SNR}_{b,u} > \beta) = P_{b,u}(\beta) P_{u,r}(\beta), \end{aligned} \quad (22)$$

which follows from Lemma 4, Corollary 1, and independent out-of-band backhaul and access links assumption. For the tUAV, (22) reduces to $P_{b,u,r}(\beta) = P_{u,r}(\beta)$ because a high capacity fiber link is assumed to reliably connect the tUAV to the core network, i.e., $P_{b,u}(\beta) = 1$ for the tUAV. Based on the above coverage performance analyses and the association policy given in (9) and (10), the overall tUAV/uUAV-assisted system coverage probabilities are given in the following theorems.

Theorem 1. *Given the association policy in (9) and (10), the tUAV-assisted system coverage probability of UEs within the hot-spot $\mathcal{D}(\mathbf{L}_o, R_o)$ is given by*

$$P^t(\beta) = \int_{-\infty}^{\infty} \left(\int_{-\infty}^{\lambda_{LoS}} E_{u,r}^{LoS} dr_u + \int_{\lambda_{LoS}}^{\infty} E_{b,r}^{LoS} dr_u + \int_{-\infty}^{\lambda_{NLoS}} E_{u,r}^{NLoS} dr_u + \int_{\lambda_{NLoS}}^{\infty} E_{b,r}^{NLoS} dr_u \right) dr_b, \quad (23)$$

where the terms are given by $\lambda_{LoS} = \left(\frac{r_b^{\alpha_b}}{\eta_{LoS}} \right)^{\frac{1}{\alpha_u}}$, $\lambda_{NLoS} = \left(\frac{r_b^{\alpha_b}}{\eta_{NLoS}} \right)^{\frac{1}{\alpha_u}}$,

$$E_{b,r}^{LoS} = \kappa_{u,r}^{LoS} P_{b,r|r_b}(\beta) f_{D'_{b,r}}(r_b) f_{D'_{u,r}|D'_{b,r}}(r_u|r_b), \quad (24)$$

$$E_{b,r}^{NLoS} = \kappa_{u,r}^{NLoS} P_{b,r|r_b}(\beta) f_{D'_{b,r}}(r_b) f_{D'_{u,r}|D'_{b,r}}(r_u|r_b), \quad (25)$$

$$E_{u,r}^{LoS} = \kappa_{u,r}^{LoS} P_{u,r|r_u}^{LoS}(\beta) f_{D'_{b,r}}(r_b) f_{D'_{u,r}|D'_{b,r}}(r_u|r_b), \text{ and} \quad (26)$$

$$E_{u,r}^{NLoS} = \kappa_{u,r}^{NLoS} P_{u,r|r_u}^{NLoS}(\beta) f_{D'_{b,r}}(r_b) f_{D'_{u,r}|D'_{b,r}}(r_u|r_b). \quad (27)$$

Proof. The proof follows directly from Lemmas 1- 4 and the association policy in (9) and (10). ■

In (23), the first and third terms correspond to the coverage probability under LoS and NLoS aerial access links, while the second and forth terms correspond to the coverage probability for the terrestrial access links. Also notice that (23) does not consider the backhaul link since $P_{b,u}(\beta) = 1$.

Theorem 2. *Given the association policy in (9) and (10), the uUAV-assisted system coverage probability of UEs within the hot-spot $\mathcal{D}(\mathbf{L}_o, R_o)$ is given by*

$$P^u(\beta) = \xi \int_{-\infty}^{\infty} \left(\int_{-\infty}^{\lambda_{LoS}} E_{b,u,r}^{LoS} dr_u + \int_{\lambda_{LoS}}^{\infty} E_{b,r}^{LoS} dr_u + \int_{-\infty}^{\lambda_{NLoS}} E_{b,u,r}^{NLoS} dr_u + \int_{\lambda_{NLoS}}^{\infty} E_{b,r}^{NLoS} dr_u \right) dr_b + (1 - \xi) P_{b,r}(\beta), \quad (28)$$

where $E_{b,u,r}^{LoS} = P_{b,u} E_{u,r}^{LoS}$ and $E_{b,u,r}^{NLoS} = P_{b,u} E_{u,r}^{NLoS}$.

Proof. The proof follows directly from Lemmas 1- 4 and the association policy in (9) and (10). ■

In (28), the first term is the coverage probability given that uUAV is available while the second term is the coverage probability over the TBS due to the unavailability of the uUAV.

IV. OPTIMAL UAV HOVERING LOCATION

The UAV deployment plays a critical role in order to maximize the overall system performance. In the previous sections, the uUAV and the tUAV system performances are analyzed for a given UAV location \mathbf{L}_u . Therefore, it is necessary to find the optimal UAV location for the maximum system coverage. Accordingly, the UAV deployment problem can be formulated for uUAV and tUAV as $P_u : \max_{\mathbf{L}_u \in \mathbb{R}^3} P^u(\beta)$ and $P_t : \max_{\mathbf{L}_u \in \mathcal{M}_n, \forall n} P^t(\beta)$, respectively. Considering the highly non-linear nature and large search space of these problems, we first narrow down the problem search space by proving that the optimal deployment location falls within a specific subspace.

Given that the hot-spot is centered at the origin and the TBS is located at $\mathbf{L}_b = \{x_b, 0, h_b\}$, one can observe the symmetry of the UAV locations around the x -axis as shown in Fig. 3. For the uUAV, we therefore only study the half space $\{y \geq 0\}$ and generalize the result for the other half without loss of generality. For the tUAV, we also study the case $y_n \geq 0$ only and generalize the findings on the other half space. We note that some part of the spherical cone \mathcal{M}_n may belong to the half space $\{y \leq 0\}$ if \mathbf{L}_n is near the x -axis [c.f Fig. 3]. In this case, the cropped spherical cone is denoted by $\bar{\mathcal{M}}_n$. We ignore the cropped part of the spherical cone since it is symmetric to a subset of the spherical cone within $\{y \geq 0\}$.

Let us define the angle and the distance between the ground projections of \mathbf{L}_n and \mathbf{L}_u as

$$\psi_u^n = \angle(\mathbf{L}_x^+, \mathbf{L}_n', \mathbf{L}_u') \text{ and} \quad (29)$$

$$R_u^n = \|\mathbf{L}_n' - \mathbf{L}_u'\|, \quad (30)$$

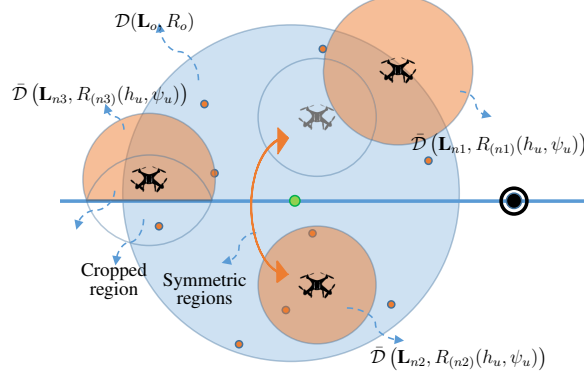


Fig. 3: Aerial view of the cone symmetry and cropped cone $\bar{\mathcal{M}}_n$ for a fixed tUAV height.

respectively. Accordingly, the spherical cone \mathcal{M}_n can be expressed by the cylindrical coordinates as

$$\mathcal{M}_n = \{R_u^n, \psi_u^n, h_u : h_u \in [h_n, h_n + T], \psi_u^n \in [0, 2\pi], R_u^n \leq R_n(h_u)\}, \quad (31)$$

where

$$R_n(h_u) = \begin{cases} (h_u - h_n) \tan(\phi) & h_u < h_n + T \cos(\phi), \\ \sqrt{T^2 - (h_u - h_n)^2} & h_u \geq h_n + T \cos(\phi) \end{cases} \quad (32)$$

represents the cone bounds for given tUAV height $h_u < h_n + T \cos(\phi)$ and the spherical bounds for $h_u \geq h_n + T \cos(\phi)$. To define the cropped spherical cone $\bar{\mathcal{M}}_n$, we need to guarantee that the distance R_u^n does not exceed the x -axis. Hence, $\bar{\mathcal{M}}_n$ is given by,

$$\bar{\mathcal{M}}_n = \{R_u^n, \psi_u^n, h_u : h_u \in [h_n, h_n + T], \psi_u^n \in [0, 2\pi], R_u^n \leq \bar{R}_n(h_u, \psi_u^n)\}, \quad (33)$$

where

$$\bar{R}_n(h_u, \psi_u^n) = \begin{cases} R_n(h_u) & \psi_u \in [0, \pi], \\ \min\left(R_n(h_u), \frac{-y_n}{\sin(\psi_u)}\right) & \psi_u \in (\pi, 2\pi), \end{cases} \quad (34)$$

is the truncated version of $R_n(h_u)$ as a result of the cropped spherical cone. In the following theorem, we prove that the optimal tUAV location belongs to a portion of the spherical cone surface.

Theorem 3. For a given GS location $\mathbf{L}_n = \{x_n, y_n \geq 0, h_n\}$ and considered user association policy, the optimal tUAV location, $\mathbf{L}_u \in \bar{\mathcal{M}}_n$, that maximizes the overall coverage performance of the hot-spot, $P^t(\beta)$, falls within the following set of locations

$$\mathcal{O}_n = \{R_u^n, \psi_u^n, h_u : h_u \in [h_n, h_n + T], \psi_u^n \in [\psi_1^n, \psi_2^n], R_u^n = \bar{R}_n(h_u, \psi_u^n)\} \in \bar{\mathcal{M}}_n, \quad (35)$$

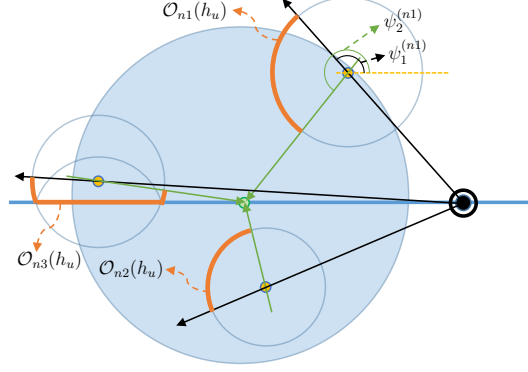


Fig. 4: The regions encompass the optimal tUAV location at a given tUAV altitude, h_u .

where $\psi_1^n = \angle(\mathbf{L}_x^+, \mathbf{L}'_b, \mathbf{L}'_n)$ and $\psi_2^n = \angle(\mathbf{L}_x^+, \mathbf{L}'_n, \mathbf{L}_o)$.

Proof. Please see Appendix E. An illustration of the set \mathcal{O}_n at a fixed h_u is shown in Fig. 4. ■

Corollary 2. For a given GS location $\mathbf{L}_n = \{x_n, y_n \geq 0, h_n\}$ and considered user association policy, the optimal uUAV location that maximizes the overall coverage performance within the hot-spot, $P^u(\beta)$ is located at $\mathbf{L}_u = \{x_u, 0, h_u\}$ such that $x_u \leq x_b$ and $h_u \geq 0$.

Proof. Please see Appendix E. ■

V. NUMERICAL ANALYSIS

In this section, we verify the mathematical analysis against independent Monte Carlo simulations and we provide insightful performance figures with respect to different system parameters and scenarios. Unless it is stated explicitly otherwise, we employ the default system parameters listed in Table II.

TABLE II: Default System Parameters.

Par.	Value	Par.	Value	Par.	Value
ρ_b / ρ_u	1 dBm	σ_n^2	-80 dBm	β	15
α_b	3	α_u	2.7	m	2
η_{LoS}/η_{NLoS}	1.6/23 dB	a_r/b_r	13/.22	a_b/b_b	7/.2
R_o	150	\mathbf{L}_b	{170, 0, 10}	T/θ_T	50m/30°

To begin with, we focus on the coverage performance of access and backhaul links for varying UAV locations $\mathbf{L}_u = \{x_u, 0, 100\}$, $x_u \in [-100, 175]$. Fig. 5 shows the coverage probabilities for the terrestrial access link TBS-RUE, $P_{b,r}$, the aerial access link tUAV-RUE, $P_{u,r}$, and the end-to-end TBS-uUAV-RUE link, $P_{b,u,r}$. As expected, the TBS link is not influenced by the UAV

location. Given that tUAV and uUAV hover at the same location, tUAV always outperforms the uUAV thanks to the high capacity wired backhaul link. For a clear comparison between tUAVs and uUAVs, let us focus on the locations where UAVs reach the maximum end-to-end coverage. The tUAV reaches the maximum coverage when hovering over the hot-spot origin because it gives the maximum access link coverage to all users which are uniformly distributed over the area of interest. On the other hand, the uUAV reaches the peak coverage at a point 50 m closer to the TBS, which is mainly because of the tradeoff between the backhaul and the access links. Since the end-to-end SNR is determined by the minimum of the access and the backhaul links, the maximum system coverage can be achieved in an equilibrium state which is obtained by getting closer to the TBS.

Furthermore, Fig. 6 shows the impact of uUAV availability under the considered user association policy. Intuitively, duty cycle of the uUAV availability ξ has a significant impact on the overall system coverage. One can observe that the maximum coverage point of the tUAV is shifted towards the negative region because users closer to the TBS are associated with the TBS. On the other hand, the maximum coverage point of the uUAV is still over the positive x -axis because the aforementioned tradeoff dominates the system behavior.

In order to explain this phenomenon, Fig. 7 shows the UEs' association regions for a UAV located at $\mathbf{L}_u = \{-75, 75, 50\}$. The users located within the orange and the yellow regions always associate with the UAV and the TBS, respectively. However, UEs fall in the blue region associate with the UAV only if there is a LoS aerial access link. Notice in Fig. 5-Fig. 7 that the tUAV and the uUAV are assumed to be located at the same location. This assumption is made for the sake of a clear demonstration of the access and the backhaul link dynamics. However, in reality, the tUAV is restricted by the tether length, inclination angle and the GS location.

In order to consider a more realistic scenario, we present the overall system coverage probabilities for the uUAV and the tUAV in Fig. 8a and 8b, respectively. To this aim, we first consider a discrete exhaustive solution approach by dividing the x - y plane into 8 m^2 grids at a fixed UAV height (100 m). Then, the coverage probability P^u is calculated at the center of each grid and displayed by means of a color map. Intuitively, the best location for the uUAV can be obtained by selecting the grid center with the maximum system coverage [c.f. Fig. 8a]. In order to alleviate the computational complexity of the exhaustive approach, Fig. 8a also shows the location calculated by the simulated annealing approach which can provide 10^{-3} coverage probability tolerance in only 20 iterations. Likewise, Fig. 8b shows the coverage probability P^t

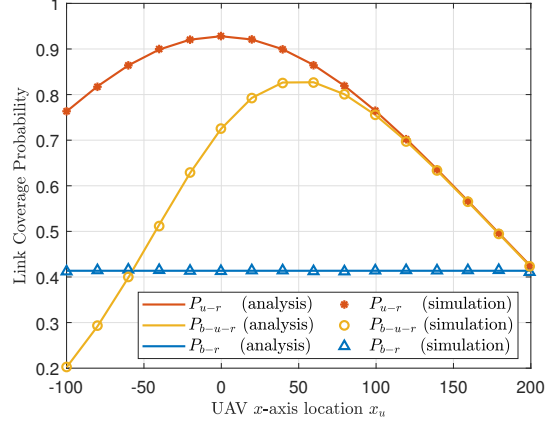


Fig. 5: The coverage probability of access and backhaul links.

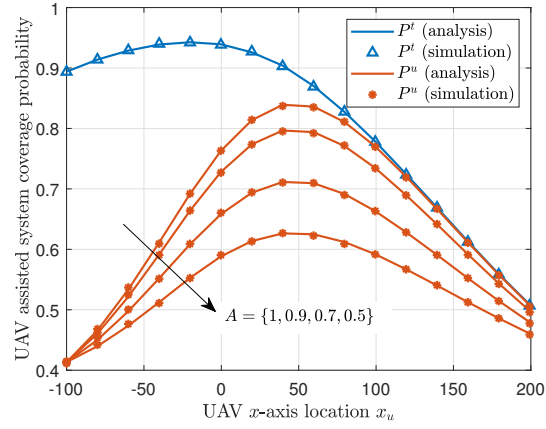


Fig. 6: P^u and P^t for different uUAV duty cycle values.

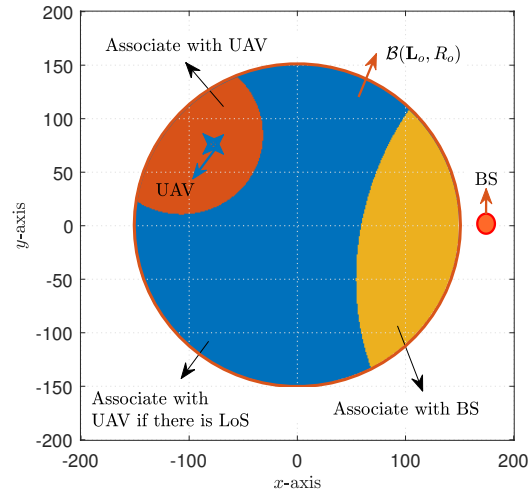
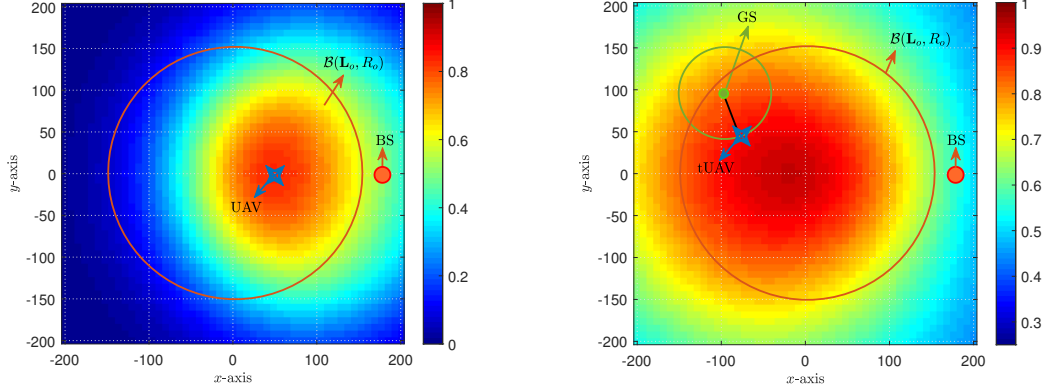


Fig. 7: User association regions based on the end-to-end average SNR.



(a) Optimal uUAV location with maximum P^u . (b) Optimal tUAV location with maximum P^t .

Fig. 8: Optimal uUAV and tUAV locations that maximize P^u and P^t .

of the tUAV for a given GS location. It is obvious that the GS location and tether length poses a significant challenge to be located at the optimal location. Moreover, Theorem 3 is numerically verified in Fig. 8b. By drawing any circle $\mathcal{C}(\mathbf{L}'_n, R_n(h_u))$ with \mathbf{L}'_n and $R_n(h_u)$ representing the GS $x - y$ location and the radius within which the tUAV can fly at the height h_u , the maximum P^t in $\mathcal{D}(\mathbf{L}'_n, R_n(h_u))$ belongs to the region described in the theorem.

Accordingly, we next compare the uUAV and tUAV coverage performance under different GS locations and availability scenarios. Based on the model developed by ITU, the average number of buildings per km^2 is given as γ_3 and the height of each building follows the Rayleigh distribution with the PDF expressed as [32],

$$f_{H_n}(h_n) = \frac{h_n}{\gamma_1^2} \exp\left(-\frac{h_n^2}{2\gamma_1^2}\right), \quad (36)$$

where γ_1 is the Rayleigh distribution parameter. For dense urban environment, $\gamma_1 = 20$ and $\gamma_3 = 300$ while for high-rise urban environment $\gamma_1 = 50$ and $\gamma_3 = 300$. Given the tether length and the percentage of accessible GSs, δ_A , the average system coverage probabilities are shown in Fig. 9a and Fig. 9b for the dense and the high-rise urban environments, respectively. The average coverage probabilities are obtained by running a Monte Carlo simulation where the location and height of the GSs are random at each iteration. For the high-rise urban environment, we set the TBS height to 30 m and approximate the environment parameters to $a_r = 22$, $b_r = 0.18$, $a_b = 11$ and $b_b = 0.16$. The optimal tUAV location is determined by using the simulated annealing search algorithm over the area described in Theorem 3. The optimal uUAV location for the dense and high-rise urban environment scenarios are obtained as $\mathbf{L}_u^* = \{48.13, 0, 109.65\}$ and $\mathbf{L}_u^* = \{48.75, 0, 147.66\}$, respectively. Fig. 9 compares the uUAV with the tUAV for parameters

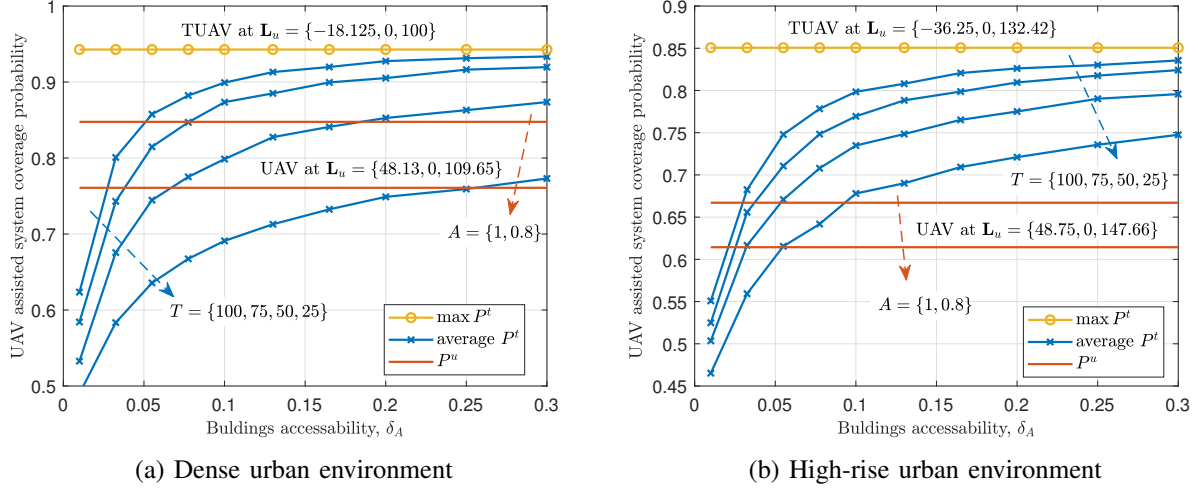


Fig. 9: The uUAV and tUAV-assisted systems performances against the percentage of accessible buildings.

$\xi \in \{0.8, 1\}$, $T \in \{25, 50, 75, 100\}$ m, and $\delta_A \in [0, 0.3]$. Thanks to increasing freedom of mobility, P^t significantly improves with higher tether length and GS accessibility. Notice that increasing T and δ_A eventually converges to the optimal case (a freely moving tUAV deployed at the optimal hovering location) where we achieve maximum P^t .

We also note that even for relatively high building accessibility, the coverage probability saturates at low values when the tether length is 25 and 50. This is because the average buildings height is 20 m for dense urban environment and therefore only 1.11% of the buildings are statistically higher than 60 m. As a result, short tethers will prevent the tUAV from reaching the optimal heights. Given a building accessibility of $\delta_A \geq 0.25$ and tether length of 100 m, the coverage performance of the tUAV-assisted system is very close to the maximum achievable coverage probability. Therefore, tether length of 100 m is in general long enough to achieve near optimal coverage probability. Both the uUAV and the tUAV-assisted systems coverage probabilities are degraded for the high-rise urban environment as compared to the dense urban environment. We also note that the tUAV system performs much better than the uUAV system for the high-rise urban environment, while the systems performance is comparable for the dense urban environment. This is due to the lower LoS probability in the high-rise urban environment and because the uUAV has to establish two A2G/G2A links to connect the RUE to the core network while the tUAV only establish one link toward the RUE.

In Fig. 10, P^t and P^u are shown with respect to the TBS x -axis location where we consider a dense urban environment with random GS locations and an accessibility factor $\delta_A = 0.3$. The

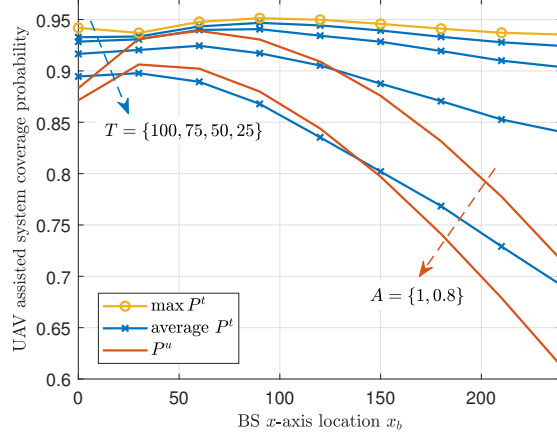


Fig. 10: P^t and P^u for varying TBS distances from the hot-spot center.

coverage probability for the uUAV and the tUAV-assisted systems are high and comparable when the TBS is near to hot-spot center. This is because the TBS has a good coverage over the hot-spot and the uUAV can cover close to the hot-spot center with desirable backhaul link conditions. As the distance between the TBS and the hot-spot center increases, the tUAV-assisted system starts significantly outperforming the uUAV-assisted system. Interestingly, the coverage probability is not maximum when the TBS is at the hot-spot center. Optimally, the TBS location is at one side of the hot-spot to serve the nearby users while the users on the other side are served by the UAV.

VI. CONCLUSIONS

In this paper, we provided a comparative performance analysis of uUAV and tUAV-assisted cellular traffic offloading from a geographical region that experiences a heavy traffic conditions. To this aim, we exploit stochastic geometry tools and derive joint distance distributions between users, the terrestrial base station (TBS), and UAV. To maximize the end-to-end signal-to-noise ratio, a user association policy is proposed as well as corresponding association regions are analytically identified. Thereafter, the overall coverage probability of uUAV/tUAV-assisted systems is obtained for given locations of the TBS and the uUAV/tUAV. Furthermore, optimal UAV location is shown to belong to the surface of the spherical cone centered at the GS. Extensive simulation results are presented to validate analytical results and compare the performance of uUAV and tUAV-assisted systems. Numerical results show that tUAV outperforms uUAV given that a sufficient number of GS location availability and tether length are provided.

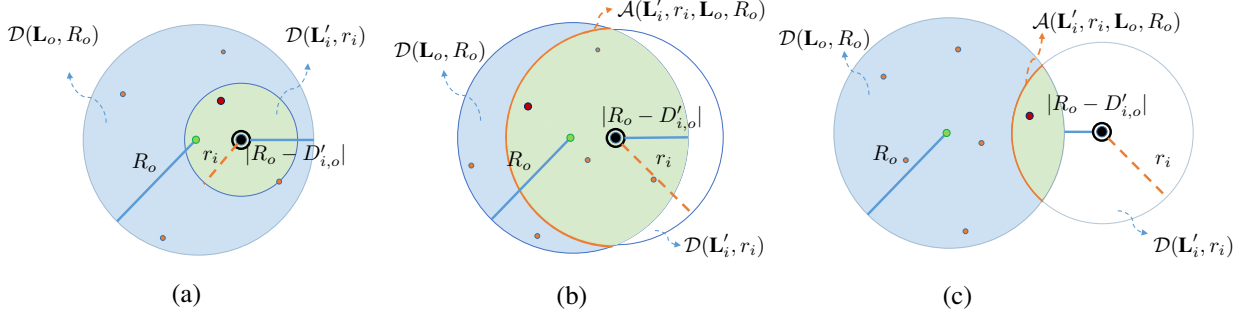


Fig. 11: Different cases for Lemma 2: a) $\mathcal{D}(\mathbf{L}'_i, r_i) \cap \mathcal{D}(\mathbf{L}_o, R_o) \equiv \mathcal{D}(\mathbf{L}'_i, r_i)$, b) $\{\mathcal{D}(\mathbf{L}'_i, r_i) \cap \mathcal{D}(\mathbf{L}_o, R_o)\} \subset \mathcal{D}(\mathbf{L}'_i, r_i)$ and $\mathbf{L}'_i \in \mathcal{D}(\mathbf{L}_o, R_o)$, and c) $\{\mathcal{D}(\mathbf{L}'_i, r_i) \cap \mathcal{D}(\mathbf{L}_o, R_o)\} \subset \mathcal{D}(\mathbf{L}'_i, r_i)$ and $\mathbf{L}'_i \notin \mathcal{D}(\mathbf{L}_o, R_o)$

APPENDIX A

LEMMA 1 PROOF

Unlike the PDF derivations in [34], [35], we consider a more general case where \mathbf{L}_i can be inside or outside $\mathcal{D}(\mathbf{L}_o, R_o)$. The cumulative distribution function (CDF) of the distance between a point \mathbf{L}'_i and a uniformly distributed RUE location within $\mathcal{D}(\mathbf{L}_o, R_o)$ is given by

$$F_{D'_{i,j}}(r_i) = \mathbb{P}(D'_{i,j} \leq r_i) = \frac{|\mathcal{D}(\mathbf{L}'_i, r_i) \cap \mathcal{D}(\mathbf{L}_o, R_o)|}{|\mathcal{D}(\mathbf{L}_o, R_o)|}. \quad (37)$$

In order to find $|\mathcal{D}(\mathbf{L}'_i, r_i) \cap \mathcal{D}(\mathbf{L}_o, R_o)|$, we consider the following two cases:

- 1) $\mathcal{D}(\mathbf{L}'_i, r_i) \cap \mathcal{D}(\mathbf{L}_o, R_o) \equiv \mathcal{D}(\mathbf{L}'_i, r_i)$: In this case, $\mathcal{D}(\mathbf{L}'_i, r_i)$ is completely inside $\mathcal{D}(\mathbf{L}_o, R_o)$ such that $0 \leq r_i \leq \max(0, R_o - D'_{i,o})$ where $D'_{i,o} = \|\mathbf{L}'_i\|$. This case is illustrated in Fig. 11a where the intersection region is highlighted by green color. Accordingly, the CDF of this case is given by the area ratio of the disks, i.e.,

$$F_{D'_{i,j}}(r_i) = \frac{\pi r_i^2}{\pi R_o^2}. \quad (38)$$

- 2) $\{\mathcal{D}(\mathbf{L}'_i, r_i) \cap \mathcal{D}(\mathbf{L}_o, R_o)\} \subset \mathcal{D}(\mathbf{L}'_i, r_i)$: In this case, a part of $\mathcal{D}(\mathbf{L}'_i, r_i)$ is outside of $\mathcal{D}(\mathbf{L}_o, R_o)$ such that $|R_o - D'_{i,o}| \leq r_i \leq R_o + D'_{i,o}$. The intersection regions of this case is illustrated in Fig. 11b and 11c for situations where $\mathbf{L}'_i \in \mathcal{D}(\mathbf{L}_o, R_o)$ and $\mathbf{L}'_i \notin \mathcal{D}(\mathbf{L}_o, R_o)$, respectively.

Accordingly, the CDF of this case is given by

$$F_{D'_{i,j}}(r_i) = \frac{\max(0, R_o - D'_{i,o})^2}{R_o^2} + \int_{|R_o - D'_{i,o}|}^{r_i} \frac{|\mathcal{A}(\mathbf{L}'_i, r_i, \mathbf{L}_o, R_o)|}{\pi R_o^2} dr_i, \quad (39)$$

where $|\mathcal{A}(\mathbf{L}'_i, r_i, \mathbf{L}_o, R_o)|$ is the arc length as shown in Fig. 11.

The arc length can be derived as follows: Let us consider two generic intersecting circles $\mathcal{C}(\mathbf{L}'_i, R'_i)$ and $\mathcal{C}(\mathbf{L}'_j, R'_j)$. Because $|\mathcal{A}(\mathbf{L}'_i, r_i, \mathbf{L}'_j, R'_j)|$ is independent from the circles' absolute locations given a fixed distance $D'_{i,j}$ from their centers, we assume $\mathbf{L}'_i = \{D'_{i,j}, 0, 0\}$

and $\mathbf{L}'_j = \{0, 0, 0\}$. Following from the mathematical definition of a circle, these circles intersect at, $\check{\mathbf{L}}_{ij} = \{\check{x}_{ij}, \check{y}_{ij}, 0\}$ and $\hat{\mathbf{L}}_{ij} = \{\hat{x}_{ij}, \hat{y}_{ij}, 0\}$ where,

$$\check{x}_{ij} = \check{x}_{ij} = \frac{(R'_i)^2 - (R'_j)^2 + (D'_{i,j})^2}{2D'_{i,j}}, \quad (40)$$

$$\check{y}_{ij} = -\hat{y}_{ij} = \sqrt{(R'_i)^2 - (\check{x}_{ij})^2}. \quad (41)$$

The angle at \mathbf{L}'_i enclosed by the lines $\mathcal{L}(\mathbf{L}'_i, \mathbf{L}'_j)$ on one side and $\mathcal{L}(\mathbf{L}'_i, \check{\mathbf{L}}_{ij})$ or $\mathcal{L}(\mathbf{L}'_i, \hat{\mathbf{L}}_{ij})$ on the other side is expressed as,

$$\phi_j = \arccos\left(\frac{\check{x}_{ij}}{R'_j}\right) = \arccos\left(\frac{R_j'^2 + (D'_{i,j})^2 - D_{i,j}'^2}{2D'_{i,j}R'_j}\right). \quad (42)$$

By use of (42), the arc length $|\mathcal{A}(\mathbf{L}'_i, r_i, \mathbf{L}'_j, R'_j)|$ is given as,

$$|\mathcal{A}(\mathbf{L}'_i, R'_j, \mathbf{L}'_j, R'_j)| = 2\phi_i R'_j = 2R'_j \arccos\left(\frac{(D'_{i,j})^2 + (R'_i)^2 - (R'_j)^2}{2D'_{i,j}R'_j}\right). \quad (43)$$

Therefore, the arc length $|\mathcal{A}(\mathbf{L}'_i, r_i, \mathbf{L}_o, R_o)|$ in (39) is expressed as,

$$|\mathcal{A}(\mathbf{L}'_i, r_i, \mathbf{L}_o, R_o)| = 2\phi_i r_i = 2r_i \arccos\left(\frac{(D'_{i,o})^2 + r_i^2 - R_o^2}{2D'_{i,o}r_i}\right). \quad (44)$$

By taking the derivate of (38) and (39) w.r.t. r_i , the PDFs can be derived from the CDFs.

APPENDIX B

LEMMA 2 PROOF

Denoting the conditional distance between the RUE and TBS by $r_b = D'_{b,r}$, we consider two cases as depicted in Fig. 12:

- 1) $r_b \leq \max(0, R_o - D'_{b,o})$: In this case, $\mathcal{D}(\mathbf{L}'_b, r_b)$ is completely inside $\mathcal{D}(\mathbf{L}_o, R_o)$ as shown in Fig. 12a. Therefore, the RUE location \mathbf{L}_r is uniformly distributed over $\mathcal{C}(\mathbf{L}'_b, r_b)$. The distance between the RUE and the UAV is bounded by $r_u \in [|D'_{b,u} - r_b|, D'_{b,u} + r_b]$. By defining the circle $\mathcal{C}(\mathbf{L}'_u, r_u)$ with $r_u \in [|D'_{b,u} - r_b|, D'_{b,u} + r_b]$, the conditional CDF of the distance $D'_{u,r}$ given $D'_{b,r}$ is expressed as,

$$F_{D'_{u,r}|D'_{b,r}}(r_u|r_b) = \mathbb{P}(D'_{u,r} < r_u|r_b) = \frac{|\mathcal{A}(\mathbf{L}'_b, r_b, \mathbf{L}'_u, r_u)|}{|\mathcal{C}(\mathbf{L}'_b, r_b)|} \quad (45)$$

$$= \frac{1}{\pi} \arccos\left(\frac{(D'_{b,u})^2 + r_b^2 - r_u^2}{2r_b D'_{b,u}}\right). \quad (46)$$

By taking the derivative w.r.t. r_u , the conditional PDF is obtained as,

$$f_{D'_{u,r}|D'_{b,r}}(r_u|r_b) = \frac{r_u}{D'_{b,u}\pi r_b} \frac{1}{\sqrt{1 - \left(\frac{(D'_{b,u})^2 + r_b^2 - r_u^2}{2D'_{b,u}r_b}\right)^2}}. \quad (47)$$

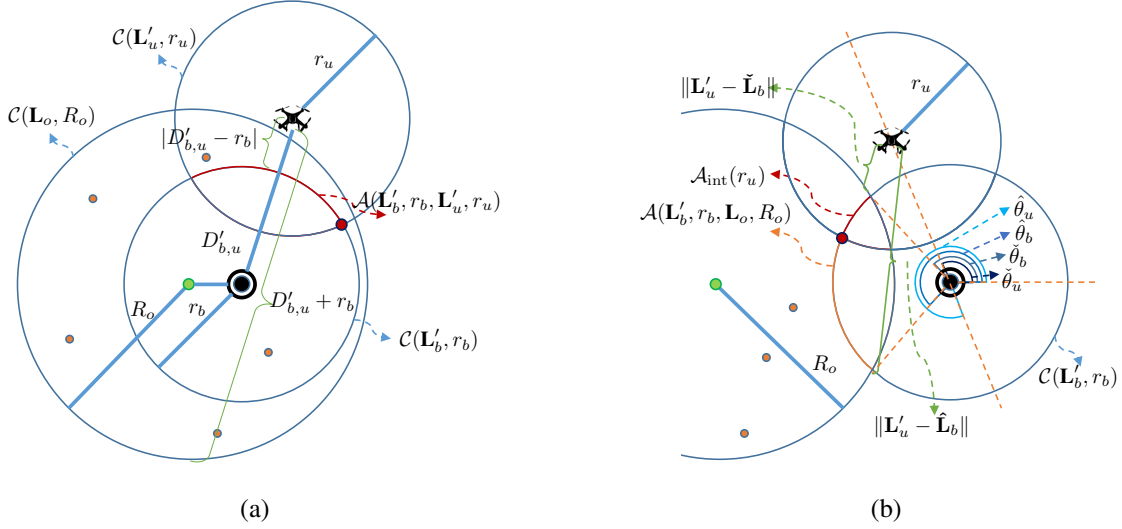


Fig. 12: Illustration of cases in Lemma 2: a) $\mathcal{D}(\mathbf{L}'_b, r_b) \cap \mathcal{D}(\mathbf{L}_o, R_o) \equiv \mathcal{D}(\mathbf{L}'_b, r_b)$, and b) $\{\mathcal{D}(\mathbf{L}'_b, r_b) \cap \mathcal{D}(\mathbf{L}_o, R_o)\} \subset \mathcal{D}(\mathbf{L}'_b, r_b)$.

2) $r_b \in [|R_o - D'_{b,o}|, R_o + D_{b,o}]$: In this case, only an arc, $\mathcal{A}(\mathbf{L}'_b, r_b, \mathbf{L}_o, R_o) \subseteq \mathcal{C}(\mathbf{L}'_b, r_b)$, is inside $\mathcal{D}(\mathbf{L}_o, R_o)$ as shown in Fig. 12b. Therefore, \mathbf{L}_r is uniformly distributed over $\mathcal{A}(\mathbf{L}'_b, r_b, \mathbf{L}_o, R_o)$. The conditional CDF $F_{D'_{u,r}|D'_{b,r}}(r_u|r_b)$ is given as,

$$F_{D'_{u,r}|D'_{b,r}}(r_u|r_b) = \mathbb{P}(D'_{u,r} < r_u|r_b) = \frac{|\mathcal{A}_{\text{int}}(r_u)|}{|\mathcal{A}(\mathbf{L}'_b, r_b, \mathbf{L}_o, R_o)|}, \quad (48)$$

where $|\mathcal{A}_{\text{int}}(r_u)| = |\mathcal{A}(\mathbf{L}'_b, r_b, \mathbf{L}'_u, r_u) \cap \mathcal{A}(\mathbf{L}'_b, r_b, \mathbf{L}_o, R_o)|$. To find $|\mathcal{A}_{\text{int}}(r_u)|$, we first define the angles $\check{\theta}_b = \angle(\mathbf{L}_x^+, \mathbf{L}'_b, \check{\mathbf{L}}_b)$, $\hat{\theta}_b = \angle(\mathbf{L}_x^+, \mathbf{L}'_b, \hat{\mathbf{L}}_b)$ with $\check{\mathbf{L}}_b$ and $\hat{\mathbf{L}}_b$ being the points of intersection between $\mathcal{C}(\mathbf{L}_o, R_o)$ and $\mathcal{C}(\mathbf{L}'_b, r_b)$, and the angles $\check{\theta}_u = \angle(\mathbf{L}_x^+, \mathbf{L}'_b, \mathbf{L}'_u)$ and $\hat{\theta}_u = (\pi + \check{\theta}_u) \bmod 2\pi$ as shown in Fig. 12b. Now we consider the following three cases for r_u ,

a) $r_u \in [|D'_{b,u} - r_b|, \|\mathbf{L}'_u - \check{\mathbf{L}}_b\|]$: if $\check{\theta}_b \leq \check{\theta}_u \leq \hat{\theta}_b$, then, $\mathcal{A}(\mathbf{L}'_b, r_b, \mathbf{L}'_u, r_u)$ and $\mathcal{A}(\mathbf{L}'_b, r_b, \mathbf{L}_o, R_o)$ completely intersect over $\mathcal{A}(\mathbf{L}'_b, r_b, \mathbf{L}'_u, r_u)$. Otherwise, $\mathcal{A}_{\text{int}}(r_u) = \emptyset$. Hence,

$$|\mathcal{A}_{\text{int}}(r_u)| = |\mathcal{A}_{\text{int}}^{(1)}(r_u)| = |\mathcal{A}(\mathbf{L}'_b, r_b, \mathbf{L}'_u, r_u)| \mathbb{1}_{\{\check{\theta}_b \leq \check{\theta}_u \leq \hat{\theta}_b\}} \quad (49)$$

By substituting (49) in (48) and taking the derivative w.r.t. r_u , $f_{D'_{u,r}|D'_{b,r}}(r_u|r_b)$ is obtained as,

$$f_{D'_{u,r}|D'_{b,r}}(r_u|r_b) = \frac{2r_u}{D'_{b,u} |\mathcal{A}(\mathbf{L}'_b, r_b, \mathbf{L}_o, R_o)|} \frac{\mathbb{1}_{\{\check{\theta}_b \leq \check{\theta}_u \leq \hat{\theta}_b\}}}{\sqrt{1 - \left(\frac{(D'_{b,u})^2 + r_b^2 - r_u^2}{2D'_{b,u}r_b} \right)^2}}. \quad (50)$$

b) $r_u \in [\|\mathbf{L}'_u - \check{\mathbf{L}}_b\|, \|\mathbf{L}'_u - \hat{\mathbf{L}}_b\|]$: The arc $\mathcal{A}(\mathbf{L}'_b, r_b, \mathbf{L}'_u, r_u)$ is symmetric around the line connecting \mathbf{L}'_b and \mathbf{L}'_u and can be split into two sides. When $r_u \in [\|\mathbf{L}'_u - \check{\mathbf{L}}_b\|, \|\mathbf{L}'_u - \hat{\mathbf{L}}_b\|]$,

the arcs $\mathcal{A}(\mathbf{L}'_b, r_b, \mathbf{L}'_u, r_u)$ and $\mathcal{A}(\mathbf{L}'_b, r_b, \mathbf{L}_o, R_o)$ intersect only from one side. Therefore, $|\mathcal{A}_{\text{int}}(r_u)|$ is equal to $|\mathcal{A}_{\text{int}}^{(1)}(\|\mathbf{L}'_u - \tilde{\mathbf{L}}_b\|)|$ plus half the difference between $|\mathcal{A}(\mathbf{L}'_b, r_b, \mathbf{L}'_u, r_u)|$ and $|\mathcal{A}(\mathbf{L}'_b, r_b, \mathbf{L}'_u, \|\mathbf{L}'_u - \tilde{\mathbf{L}}_b\|)|$. Hence,

$$|\mathcal{A}_{\text{int}}(r_u)| = |\mathcal{A}_{\text{int}}^{(2)}(r_u)| = |\mathcal{A}_{\text{int}}^{(1)}(\|\mathbf{L}'_u - \tilde{\mathbf{L}}_b\|)| + \frac{1}{2}|\mathcal{A}(\mathbf{L}'_b, r_b, \mathbf{L}'_u, r_u)| - \frac{1}{2}|\mathcal{A}(\mathbf{L}'_b, r_b, \mathbf{L}'_u, \|\mathbf{L}'_u - \tilde{\mathbf{L}}_b\|)|. \quad (51)$$

By substituting (51) in (48) and taking the derivative w.r.t. r_u , $f_{D'_{b,u}|D'_{b,r}}(r_u|r_b)$ is obtained as,

$$f_{D'_{b,u}|D'_{b,r}}(r_u|r_b) = \frac{r_u}{D'_{b,u}|\mathcal{A}(\mathbf{L}'_b, r_b, \mathbf{L}_o, R_o)|} \frac{1}{\sqrt{1 - \left(\frac{(D'_{b,u})^2 + r_b^2 - r_u^2}{2D'_{b,u}r_b}\right)^2}}. \quad (52)$$

c) $r_u \in [\|\mathbf{L}'_u - \hat{\mathbf{L}}_b\|, D'_{b,u} + r_b]$: when $r_u \in [\|\mathbf{L}'_u - \hat{\mathbf{L}}_b\|, D'_{b,u} + r_b]$, the arcs $\mathcal{A}(\mathbf{L}'_b, r_b, \mathbf{L}'_u, r_u)$ and $\mathcal{A}(\mathbf{L}'_b, r_b, \mathbf{L}_o, R_o)$ intersect only if $\{\tilde{\theta}_b \leq \hat{\theta}_u \leq \hat{\theta}_b\}$. Therefore,

$$|\mathcal{A}_{\text{int}}(r_u)| = |\mathcal{A}_{\text{int}}^{(3)}(r_u)| = |\mathcal{A}_{\text{int}}^{(2)}(\|\mathbf{L}'_u - \hat{\mathbf{L}}_b\|)| + \left(|\mathcal{A}(\mathbf{L}'_b, r_b, \mathbf{L}'_u, r_u)| - |\mathcal{A}(\mathbf{L}'_b, r_b, \mathbf{L}'_u, \|\mathbf{L}'_u - \hat{\mathbf{L}}_b\|)| \right) \mathbb{1}_{\{\tilde{\theta}_b \leq \hat{\theta}_u \leq \hat{\theta}_b\}}. \quad (53)$$

By substituting (53) in (48) and taking the derivative w.r.t. r_u , $f_{D'_{b,u}|D'_{b,r}}(r_u|r_b)$ is obtained as,

$$f_{D'_{b,u}|D'_{b,r}}(r_u|r_b) = \frac{2r_u}{D'_{b,u}|\mathcal{A}(\mathbf{L}'_b, r_b, \mathbf{L}_o, R_o)|} \frac{\mathbb{1}_{\{\tilde{\theta}_b \leq \hat{\theta}_u \leq \hat{\theta}_b\}}}{\sqrt{1 - \left(\frac{(D'_{b,u})^2 + r_b^2 - r_u^2}{2D'_{b,u}r_b}\right)^2}}. \quad (54)$$

Combining all cases, Lemma 2 is proved.

APPENDIX C

LEMMA 3 PROOF

The Rayleigh fading channel coverage probability from the TBS is derived as follows,

$$\begin{aligned} P_{b,r}(\beta) &\stackrel{(a)}{=} \mathbb{P}(\text{SNR}_{b,r} > \beta), \\ &\stackrel{(b)}{=} \mathbb{E}_{D'_{b,r}} \left[\mathbb{P} \left(G_b > \bar{\beta}_b ((D'_{b,r})^2 + h_b^2)^{\alpha_b/2} | D'_{b,r} \right) \right], \\ &\stackrel{(c)}{=} \mathbb{E}_{D'_{b,r}} \left[\exp \left(-\bar{\beta}_b ((D'_{b,r})^2 + h_b^2)^{\alpha_b/2} \right) \right], \\ &\stackrel{(d)}{=} \int_{-\infty}^{\infty} \exp \left(-\bar{\beta}_b (r_b^2 + h_b^2)^{\alpha_b/2} \right) f_{D'_{b,r}}(r_b) dr_b. \end{aligned}$$

where (a) follows from the coverage probability definition, (b) follows by substituting $SNR_{b,r}$ from (2) with $\bar{\beta}_b = \frac{\sigma_n^2 \beta}{\rho_b}$, (c) follows from the CCDF of G_b , and (d) follows from the expectation over $D'_{b,r}$.

APPENDIX D

LEMMA 4 PROOF

The Nakagami- m fading channel coverage probability from the UAV to the RUE is derived as follows,

$$\begin{aligned}
P_{u,r}(\beta) &= \mathbb{P}(\text{SNR} > \beta) = \mathbb{E}_{D'_{u,r}, \eta_i} \left[\mathbb{P} \left(G_{u,r} > \bar{\beta}_u ((D'_{u,r})^2 + h_u^2)^{\alpha_u/2} \eta_i | D'_{u,r}, \eta_i \right) \right], \\
&\stackrel{(a)}{=} \mathbb{E}_{D'_{u,r}, \eta_i} \left[\frac{\Gamma(m, m\bar{\beta}_u ((D'_{u,r})^2 + h_u^2)^{\alpha_u/2} \eta_i)}{\Gamma(m)} \right], \\
&\stackrel{(b)}{=} \mathbb{E}_{D'_{u,r}, \eta_i} \left[\sum_{k=0}^{m-1} \frac{(m\bar{\beta}_u ((D'_{u,r})^2 + h_u^2)^{\alpha_u/2} \eta_i)^k}{k!} \exp \left(-m\bar{\beta}_u ((D'_{u,r})^2 + h_u^2)^{\alpha_u/2} \eta_i \right) \right], \\
&= \mathbb{E}_{D'_{u,r}} \left[\sum_{i \in \{\text{LoS}, \text{NLoS}\}} \kappa_{u,r}^i \sum_{k=0}^{m-1} \frac{(m\bar{\beta}_u ((D'_{u,r})^2 + h_u^2)^{\alpha_u/2} \eta_i)^k}{k!} \exp \left(-m\bar{\beta}_u ((D'_{u,r})^2 + h_u^2)^{\alpha_u/2} \eta_i \right) \right], \\
&\stackrel{(c)}{=} \int_{-\infty}^{\infty} \sum_{i \in \{\text{LoS}, \text{NLoS}\}} \kappa_{u,r}^i \sum_{k=0}^{m-1} \frac{(m\bar{\beta}_u (r_u^2 + h_u^2)^{\alpha_u/2} \eta_i)^k}{k!} \exp \left(-m\bar{\beta}_u (r_u^2 + h_u^2)^{\alpha_u/2} \eta_i \right) f_{D'_{u,r}}(r_u) dr_u.
\end{aligned}$$

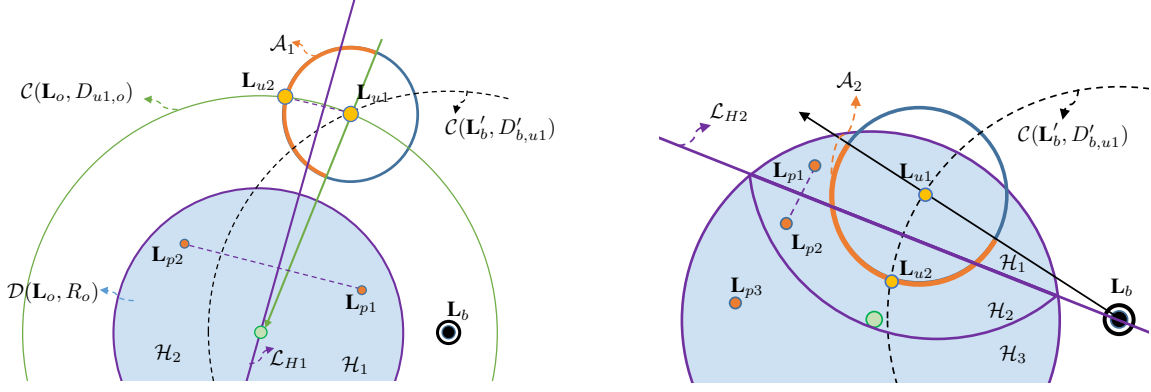
where (a) follows from the CCDF of $G_{u,r}$, (b) follows from the incomplete gamma function definition for $m \in \mathbb{Z}^+$, and (c) follows from the expectation over $D'_{u,r}$.

APPENDIX E

THEOREM 3 PROOF

For a given GS, the maximum coverage probability is obtained by placing the tUAV at the optimal location on the (cropped) spherical cone, $\bar{\mathcal{M}}_n$. By fixing the tUAV hovering height at $h_u \in [h_n, h_n + T]$, the tUAV can fly within the (cropped) desk, $\bar{\mathcal{D}}(\mathbf{L}_n, \bar{R}_n(h_u, \psi_u^n))$.

To prove Theorem 3, we prove the following *two claims*: (1) As the tUAV moves far from the TBS with a constant distance from \mathbf{L}_o , the coverage probability P^t is improved. Hence, the optimal tUAV location belongs to \mathcal{A}_1 as shown in Fig. 13a. (2) As the tUAV moves closer to \mathbf{L}_o with a constant distance from the TBS, P^t is also improved. As a result, the optimal tUAV location belongs to \mathcal{A}_2 as shown in Fig. 13b. The intersection region, $\mathcal{A}_1 \cap \mathcal{A}_2$, $\forall h_u \in [h_n, h_n + T]$ is \mathcal{O}_n as described in Theorem 3. Therefore, by proving these two claims, Theorem 3 is proved. The *two claims* are proved as follows:



(a) Comparison between two tUAV locations at the same distance from \mathbf{L}_o but different distances from \mathbf{L}_b . (b) Comparison between two tUAV locations at the same distance from \mathbf{L}_b but different distances from \mathbf{L}_o .

Fig. 13: Optimal tUAV location at a given height.

1) Compare P^t at two tUAV locations, \mathbf{L}_{u1} and \mathbf{L}_{u2} , with same distances from \mathbf{L}_o , $D_{u1,o} = D_{u2,o}$ but different distances from the TBS, $D_{b,u1} < D_{b,u2}$. We divide $\mathcal{D}(\mathbf{L}_o, R_o)$ into two halves, \mathcal{H}_1 and \mathcal{H}_2 , by a hypothetical line where $\overline{\text{SNR}}_{u1,r} = \overline{\text{SNR}}_{u2,r}$ for any RUE on the line, this line is denoted as \mathcal{L}_{H1} (see Fig. 13a). For any user location $\mathbf{L}_{p1} \in \mathcal{H}_1$, there is another user location (with same probability) such that $\mathbf{L}_{p2} \in \mathcal{H}_2$ and, \mathbf{L}_{p1} and \mathbf{L}_{p2} are symmetric around \mathcal{L}_{H1} . We note that $P_{b,r}(p_1) \geq P_{b,r}(p_2)$, $P_{u1,r}(p_2) = P_{u2,r}(p_1)$, $P_{u1,r}(p_1) = P_{u2,r}(p_2)$ and $P_{u1,r}(p_2) \leq P_{u1,r}(p_1)$ where $P_{i,j}(p_k)$ is the i - j link coverage probability for a point located at \mathbf{L}_{p_k} . Now, compare P^t for the tUAV locations \mathbf{L}_{u1} and \mathbf{L}_{u2} for all the possible six cases:

- a) $P_{b,r}(p_2) < P_{u1,r}(p_1)$: The users at p_1 and p_2 are served by the TBS whether the tUAV is at \mathbf{L}_{u1} and \mathbf{L}_{u2} . Therefore, $P^t(p_1) = P_{b,r}(p_1)$ and $P^t(p_2) = P_{b,r}(p_2)$.
- b) $P_{b,r}(p_1) \geq P_{u1,r}(p_1) \geq P_{b,r}(p_2) \geq P_{u1,r}(p_2)$:
 - tUAV at \mathbf{L}_{u1} : $P^t(p_1) = P_{b,r}(p_1)$, and, $P^t(p_2) = P_{b,r}(p_2)$.
 - tUAV at \mathbf{L}_{u2} : $P^t(p_1) = P_{b,r}(p_1)$, and, $P^t(p_2) = P_{u2,r}(p_2) > P_{b,r}(p_2)$.
- c) $P_{b,r}(p_1) \geq P_{u1,r}(p_1) \geq P_{u1,r}(p_2) \geq P_{b,r}(p_2)$:
 - tUAV at \mathbf{L}_{u1} : $P^t(p_1) = P_{b,r}(p_1)$, and, $P^t(p_2) = P_{u1,r}(p_2)$.
 - tUAV at \mathbf{L}_{u2} : $P^t(p_1) = P_{b,r}(p_1)$, and, $P^t(p_2) = P_{u2,r}(p_2) > P_{u1,r}(p_2)$.
- d) $P_{u1,r}(p_1) \geq P_{b,r}(p_1) \geq P_{u1,r}(p_2) \geq P_{b,r}(p_2)$:
 - tUAV at \mathbf{L}_{u1} : $P^t(p_1) = P_{u1,r}(p_1)$, and, $P^t(p_2) = P_{u1,r}(p_2)$.
 - tUAV at \mathbf{L}_{u2} : $P^t(p_1) = P_{b,r}(p_1) \geq P_{u1,r}(p_2)$. And, $P^t(p_2) = P_{u2,r}(p_2) = P_{u1,r}(p_1)$.
- e) $P_{u1,r}(p_1) \geq P_{b,r}(p_1) \geq P_{b,r}(p_2) \geq P_{u1,r}(p_2)$:

- tUAV at \mathbf{L}_{u1} : $P^t(p_1) = P_{u1,r}(p_1)$, and, $P^t(p_2) = P_{b,r}(p_2)$.
 - tUAV at \mathbf{L}_{u2} : $P^t(p_1) = P_{b,r}(p_1) \geq P_{b,r}(p_2)$, and, $P^t(p_2) = P_{u2,r}(p_2) = P_{u1,r}(p_1)$.
- f) $P_{u1,r}(p_1) \geq P_{u2,r}(p_2) \geq P_{b,r}(p_1) \geq P_{b,r}(p_2)$:
- tUAV at \mathbf{L}_{u1} : $P^t(p_1) = P_{u1,r}(p_1)$, and, $P^t(p_2) = P_{u1,r}(p_2)$.
 - tUAV at \mathbf{L}_{u2} : $P^t(p_1) = P_{u2,r}(p_1) = P_{u1,r}(p_2)$, and, $P^t(p_2) = P_{u2,r}(p_2) = P_{u1,r}(p_1)$.

In all the cases, the overall coverage probability P^t is enhanced or unchanged when the tUAV is located at \mathbf{L}_{u2} as compared with \mathbf{L}_{u1} , which proves the first claim.

- 2) Compare P^t at two tUAV locations, \mathbf{L}_{u1} and \mathbf{L}_{u2} , with same distances from the TBS, $D_{b,u1} = D_{b,u2}$ but different distances from \mathbf{L}_o , $D_{u1,o} > D_{u2,o}$. We draw a hypothetical line, denoted as \mathcal{L}_{H2} , where $\overline{\text{SNR}}_{u1,r} = \overline{\text{SNR}}_{u2,r}$ at any RUE on the line (see Fig. 13b). Since $D_{b,u1} = D_{b,u2}$, the line passes through the TBS as Fig. 13b shows. Let $\mathcal{D}(\mathbf{L}_o, R_o) = \mathcal{H}_1 \cup \mathcal{H}_2 \cup \mathcal{H}_3$ where \mathcal{H}_1 is the smaller part of $\mathcal{D}(\mathbf{L}_o, R_o)$ that is on one side of \mathcal{L}_{H2} , \mathcal{H}_2 is symmetric to \mathcal{H}_1 around \mathcal{L}_{H2} and $\mathcal{H}_3 = \mathcal{D}(\mathbf{L}_o, R_o) \setminus (\mathcal{H}_1 \cup \mathcal{H}_2)$ (see Fig. 13b). If \mathcal{L}_{H2} does not intersect with $\mathcal{D}(\mathbf{L}_o, R_o)$, then $\mathcal{H}_1 = \emptyset$, $\mathcal{H}_2 = \emptyset$ and $\mathcal{H}_3 = \mathcal{D}(\mathbf{L}_o, R_o)$.

For any user location $\mathbf{L}_{p1} \in \mathcal{H}_1$, there is another user location (with same probability) such that $\mathbf{L}_{p2} \in \mathcal{H}_2$ where \mathbf{L}_{p1} and \mathbf{L}_{p2} are symmetric around \mathcal{L}_{H2} . We note that $P_{b,r}(p_1) = P_{b,r}(p_2)$, and $P_{u1,r}(p_1) = P_{u2,r}(p_2)$ and $P_{u1,r}(p_2) = P_{u2,r}(p_1)$. In each of the following cases,

- $P_{b,r}(p_1) > P_{u1,r}(p_1)$,
- $P_{b,r}(p_1) < P_{u1,r}(p_2)$,
- $P_{u1,r}(p_2) < P_{b,r}(p_1) < P_{u1,r}(p_1)$,

the same coverage probability over the region $\mathcal{H}_1 \cup \mathcal{H}_2$ is obtained whether the tUAV is placed at \mathbf{L}_{u1} or \mathbf{L}_{u2} . However, if the RUE is located at $\mathbf{L}_{p3} \in \mathcal{H}_3$, the coverage probability at \mathbf{L}_{p3} can be computed as follows:

- a) If $P_{b,r}(p_3) > P_{u2,r}(p_3)$: The user associates with the TBS in all cases. Therefore, $P^t(p_3) = P_{b,r}(p_3)$ whether the tUAV located at \mathbf{L}_{u1} or \mathbf{L}_{u2} .
- b) If $P_{b,r}(p_3) < P_{u1,r}(p_3)$: The user associates with the tUAV in all cases. Therefore,
- tUAV at \mathbf{L}_{u1} : $P^t(p_3) = P_{u1,r}(p_3)$.
 - tUAV at \mathbf{L}_{u2} : $P^t(p_3) = P_{u2,r}(p_3) > P_{u1,r}(p_3)$.
- c) If $P_{u1,r}(p_3) < P_{b,r}(p_3) < P_{u2,r}(p_3)$: Consider the tUAV locations \mathbf{L}_{u1} and \mathbf{L}_{u2} as follows,
- tUAV at \mathbf{L}_{u1} : $P^t(p_3) = P_{b,r}(p_3)$.

- tUAV at \mathbf{L}_{u2} : $P^t(p_3) = P_{u2,r}(p_1) \geq P_{b,r}(p_3)$.

Therefore, the overall coverage probability P^t is enhanced or unchanged when the tUAV is located at \mathbf{L}_{u2} as compared with \mathbf{L}_{u1} which proves the second claim. In case of uUAV, P^u is a function of the link quality between the uUAV and the TBS. Therefore, the first part of the above proof cannot be used. Based on the second part, where the distance between the UAV and the TBS is fixed at $D_{b,u}$, we note that P^u is maximized when the uUAV is located at $\mathbf{L}_u = \{x_u, 0, h_u\}$ where $x_u = x_b - D_{b,u}$, $\forall D_{b,u} \geq 0$ and $\forall h_u \geq 0$.

REFERENCES

- [1] X. Cao, P. Yang, M. Alzenad, X. Xi, D. Wu, and H. Yanikomeroglu, "Airborne communication networks: A survey," *IEEE Journal on Selected Areas in Communications*, vol. 36, no. 9, pp. 1907–1926, Sep. 2018.
- [2] A. Fotouhi, H. Qiang, M. Ding, M. Hassan, L. G. Giordano, A. Garcia-Rodriguez, and J. Yuan, "Survey on UAV cellular communications: Practical aspects, standardization advancements, regulation, and security challenges," *IEEE Communications Surveys Tutorials*, vol. 21, no. 4, pp. 3417–3442, Fourthquarter 2019.
- [3] M. Mozaffari, W. Saad, M. Bennis, Y. Nam, and M. Debbah, "A tutorial on UAVs for wireless networks: Applications, challenges, and open problems," *IEEE Communications Surveys Tutorials*, vol. 21, no. 3, pp. 2334–2360, thirdquarter 2019.
- [4] H. Zhang, L. Song, and Z. Han, *UAV Assisted Cellular Communications*, pp. 61–100, Springer International Publishing, Cham, 2020.
- [5] J. Chen, U. Mitra, and D. Gesbert, "Optimal UAV relay placement for single user capacity maximization over terrain with obstacles," in *2019 IEEE 20th International Workshop on Signal Processing Advances in Wireless Communications (SPAWC)*, July 2019, pp. 1–5.
- [6] N. Kouzayha, H. ElSawy, H. Dahrouj, K. Alshaikh, T. Y. Al-Naffouri, and M.-S. Alouini, "Stochastic geometry analysis of hybrid aerial terrestrial networks with mmWave backhauling," 2019, Available online: <https://arxiv.org/abs/1910.12035>.
- [7] M. M. Azari, F. Rosas, and S. Pollin, "Cellular connectivity for UAVs: Network modeling, performance analysis, and design guidelines," *IEEE Transactions on Wireless Communications*, vol. 18, no. 7, pp. 3366–3381, July 2019.
- [8] O. M. Bushnaq, A. Celik, H. ElSawy, M.-S. Alouini, and T. Y. Al-Naffouri, "Aerial data aggregation in IoT networks: Hovering & traveling time dilemma," in *2018 IEEE Global Communications Conference*, Dec 2018, vol. Abu-Dhabi, UAE.
- [9] O. M. Bushnaq, A. Celik, H. ElSawy, M.-S. Alouini, and T. Y. Al-Naffouri, "Aeronautical data aggregation and field estimation in IoT networks: Hovering and traveling time dilemma of UAVs," *IEEE Transactions on Wireless Communications*, vol. 18, no. 10, pp. 4620–4635, Oct 2019.
- [10] J. Gong, T. Chang, C. Shen, and X. Chen, "Flight time minimization of UAV for data collection over wireless sensor networks," *IEEE Journal on Selected Areas in Communications*, vol. 36, no. 9, pp. 1942–1954, Sep. 2018.
- [11] H. Zhang, L. Song, and Z. Han, *Cellular Assisted UAV Sensing*, pp. 101–221, Springer International Publishing, Cham, 2020.
- [12] M. A. Kishk, A. Bader, and M.-S. Alouini, "Capacity and coverage enhancement using long-endurance tethered airborne base stations," 2019, Available online: <https://arxiv.org/abs/1906.11559>.
- [13] M. A. Kishk, A. Bader, and M.-S. Alouini, "On the 3-D placement of airborne base stations using tethered UAVs," 2019, Available online: <https://arxiv.org/abs/1907.04299>.

- [14] Y. Zeng and R. Zhang, "Energy-efficient UAV communication with trajectory optimization," *IEEE Transactions on Wireless Communications*, vol. 16, no. 6, pp. 3747–3760, June 2017.
- [15] M. Alzenad, A. El-Keyi, F. Lagum, and H. Yanikomeroglu, "3-D placement of an unmanned aerial vehicle base station (UAV-BS) for energy-efficient maximal coverage," *IEEE Wireless Communications Letters*, vol. 6, no. 4, pp. 434–437, Aug 2017.
- [16] D. Zorbas, L. D. P. Pugliese, T. Razafindralambo, and F. Guerriero, "Optimal drone placement and cost-efficient target coverage," *Journal of Network and Computer Applications*, vol. 75, pp. 16 – 31, 2016.
- [17] Y. Zeng, J. Xu, and R. Zhang, "Energy minimization for wireless communication with rotary-wing UAV," *IEEE Transactions on Wireless Communications*, vol. 18, no. 4, pp. 2329–2345, April 2019.
- [18] Y. Li and L. Cai, "UAV-assisted dynamic coverage in a heterogeneous cellular system," *IEEE Network*, vol. 31, no. 4, pp. 56–61, July 2017.
- [19] M. Erdelj, O. Saif, E. Natalizio, and I. Fantoni, "UAVs that fly forever: Uninterrupted structural inspection through automatic UAV replacement," *Ad Hoc Networks*, vol. 94, pp. 101612, 2019.
- [20] V. Sharma, K. Srinivasan, H.-C. Chao, K.-L. Hua, and W.-H. Cheng, "Intelligent deployment of UAVs in 5G heterogeneous communication environment for improved coverage," *Journal of Network and Computer Applications*, vol. 85, pp. 94 – 105, 2017, Intelligent Systems for Heterogeneous Networks.
- [21] J. Lyu, Y. Zeng, R. Zhang, and T. J. Lim, "Placement optimization of UAV-mounted mobile base stations," *IEEE Communications Letters*, vol. 21, no. 3, pp. 604–607, March 2017.
- [22] R. I. Bor-Yaliniz, A. El-Keyi, and H. Yanikomeroglu, "Efficient 3-D placement of an aerial base station in next generation cellular networks," in *2016 IEEE International Conference on Communications (ICC)*, May 2016, pp. 1–5.
- [23] Y. Chen, W. Feng, and G. Zheng, "Optimum placement of UAV as relays," *IEEE Communications Letters*, vol. 22, no. 2, pp. 248–251, Feb 2018.
- [24] B. Galkin, J. Kibilda, and L. A. DaSilva, "A stochastic model for UAV networks positioned above demand hotspots in urban environments," *IEEE Transactions on Vehicular Technology*, vol. 68, no. 7, pp. 6985–6996, July 2019.
- [25] M. Alzenad, M. Z. Shakir, H. Yanikomeroglu, and M. Alouini, "FSO-based vertical backhaul/fronthaul framework for 5G+ wireless networks," *IEEE Communications Magazine*, vol. 56, no. 1, pp. 218–224, Jan 2018.
- [26] C. T. Cicek, H. Gultekin, B. Tavli, and H. Yanikomeroglu, "Backhaul-aware optimization of UAV base station location and bandwidth allocation for profit maximization," 2018, Available online: <https://arxiv.org/abs/1810.12395>.
- [27] M. Y. Selim and A. E. Kamal, "Post-disaster 4G/5G network rehabilitation using drones: Solving battery and backhaul issues," in *2018 IEEE Globecom Workshops (GC Wkshps)*, Dec 2018, pp. 1–6.
- [28] H. ElSawy, E. Hossain, and M. Haenggi, "Stochastic geometry for modeling, analysis, and design of multi-tier and cognitive cellular wireless networks: A survey," *IEEE Communications Surveys Tutorials*, vol. 15, no. 3, pp. 996–1019, Third 2013.
- [29] H. ElSawy, A. Sultan-Salem, M. Alouini, and M. Z. Win, "Modeling and analysis of cellular networks using stochastic geometry: A tutorial," *IEEE Communications Surveys Tutorials*, vol. 19, no. 1, pp. 167–203, Firstquarter 2017.
- [30] M. Haenggi, J. G. Andrews, F. Baccelli, O. Dousse, and M. Franceschetti, "Stochastic geometry and random graphs for the analysis and design of wireless networks," *IEEE Journal on Selected Areas in Communications*, vol. 27, no. 7, pp. 1029–1046, Sep. 2009.
- [31] ITU-R, "Propagation data and prediction methods required for the design of terrestrial broadband radio access systems operating in a frequency range from 3 to 60 GHz," *ITU-R*, February 2012.
- [32] A. Al-Hourani, S. Kandeepan, and S. Lardner, "Optimal LAP altitude for maximum coverage," *IEEE Wireless Communications Letters*, vol. 3, no. 6, pp. 569–572, Dec 2014.

- [33] M. K. Simon and M.-S. Alouini, *Digital Communication over Fading Channels*, vol. 95, John Wiley & Sons, 2005.
- [34] M. Afshang and H. S. Dhillon, “Fundamentals of modeling finite wireless networks using binomial point process,” *IEEE Transactions on Wireless Communications*, vol. 16, no. 5, pp. 3355–3370, May 2017.
- [35] V. V. Chetlur and H. S. Dhillon, “Downlink coverage analysis for a finite 3-D wireless network of unmanned aerial vehicles,” *IEEE Transactions on Communications*, vol. 65, no. 10, pp. 4543–4558, Oct 2017.